Calhoun: The NPS Institutional Archive

DSpace Repository

Theses and Dissertations | 1. Thesis and Dissertation Collection, all items

2005

Impact of leading-edge orientation and shape on performance of a compressor blade

Powell, Jonathan D.

Monterey, California. Naval Postgraduate School

http://hdl.handle.net/10945/1867

This publication is a work of the U.S. Government as defined in Title 17, United States Code, Section 101. Copyright protection is not available for this work in the United States.

Downloaded from NPS Archive: Calhoun

Calhoun is the Naval Postgraduate School's public access digital repository for research materials and institutional publications created by the NPS community. Calhoun is named for Professor of Mathematics Guy K. Calhoun, NPS's first appointed -- and published -- scholarly author.

Dudley Knox Library / Naval Postgraduate School
411 Dyer Road / 1 University Circle
Monterey, California USA 93943

http://www.nps.edu/library

NAVAL POSTGRADUATE SCHOOL

MONTEREY, CALIFORNIA

THESIS

IMPACT OF LEADING-EDGE ORIENTATION AND SHAPE ON PERFORMANCE OF COMPRESSOR BLADES

by

Jonathan D. Powell

June 2005

Thesis Advisor:	Knox Millsaps
Second Reader:	Garth Hobson

Approved for public release; distribution is unlimited

THIS PAGE INTENTIONALLY LEFT BLANK

REPORT DOCUMENTATION PAGE			Form Approved OMB No. 0704-0188
Public reporting burden for this collection of information is estimated to average 1 hour per response, including the time for reviewing instruction, searching existing data sources, gathering and maintaining the data needed, and completing and reviewing the collection of information. Send comments regarding this burden estimate or any other aspect of this collection of information, including suggestions for reducing this burden, to Washington headquarters Services, Directorate for Information Operations and Reports, 1215 Jefferson Davis Highway, Suite 1204, Arlington, VA 22202-4302, and to the Office of Management and Budget, Paperwork Reduction Project (0704-0188) Washington DC 20503.			
1. AGENCY USE ONLY *(Leave blank)*	**2. REPORT DATE** June 2005	**3. REPORT TYPE AND DATES COVERED** Master's Thesis	
4. TITLE AND SUBTITLE: Impact of Leading-Edge Orientation and Shape on Performance of Compressor Blades			**5. FUNDING NUMBERS**
6. AUTHOR(S) Jonathan D. Powell			
7. PERFORMING ORGANIZATION NAME(S) AND ADDRESS(ES) Naval Postgraduate School Monterey, CA 93943-5000			**8. PERFORMING ORGANIZATION REPORT NUMBER**
9. SPONSORING /MONITORING AGENCY NAME(S) AND ADDRESS(ES) N/A			**10. SPONSORING/MONITORING AGENCY REPORT NUMBER**
11. SUPPLEMENTARY NOTES The views expressed in this thesis are those of the author and do not reflect the official policy or position of the Department of Defense or the U.S. Government.			
12a. DISTRIBUTION / AVAILABILITY STATEMENT Approved for public release; distribution is unlimited			**12b. DISTRIBUTION CODE**
13. ABSTRACT (maximum 200 words) This thesis presents a Computation Fluid Dynamics (CFD) analysis of the aerodynamic performance of circular and elliptical leading edges of compressor blades, with a range of leading-edge droop angles. Specifically, simulations were conducted, with a free stream Mach number of 0.65 to quantify the change in pressure distributions and boundary layer momentum thickness in the leading edge region for a range of incidences on a flat plate with various leading-edge ellipticity ratios, ranging from unity (circular) to 5.5. In addition, the impact of drooping the leading edge was analyzed over a range of incidence angles from zero to 13 degrees. Pressure distributions indicate that elliptical leading edges can eliminate separation bubbles at zero incidence. The results indicated that the minimum loss occurred at an ellipticity ratio of about 3 and elliptical leading edges with a droop slightly greater than the average incidence can significantly decreased aerodynamic losses over a wider range of incidences.			
14. SUBJECT TERMS Leading Edge Direction, Leading Edge Shape, Separation Bubble, Computational Fluid Dynamics, Drooped Leading Edge, Ellipticity Ratio			**15. NUMBER OF PAGES** 95
			16. PRICE CODE
17. SECURITY CLASSIFICATION OF REPORT Unclassified	**18. SECURITY CLASSIFICATION OF THIS PAGE** Unclassified	**19. SECURITY CLASSIFICATION OF ABSTRACT** Unclassified	**20. LIMITATION OF ABSTRACT** UL

NSN 7540-01-280-5500

Standard Form 298 (Rev. 2-89)
Prescribed by ANSI Std. 239-18

THIS PAGE INTENTIONALLY LEFT BLANK

Approved for public release; distribution is unlimited

IMPACT OF LEADING-EDGE ORIENTATION AND SHAPE ON PERFORMANCE OF A COMPRESSOR BLADE

Jonathan D. Powell
Ensign, United States Navy
B.S., United States Naval Academy, 2004

Submitted in partial fulfillment of the
requirements for the degree of

MASTER OF SCIENCE IN MECHANICAL ENGINEERING

from the

NAVAL POSTGRADUATE SCHOOL
June 2005

Author: Jonathan D. Powell

Approved by: Knox T. Millsaps
Thesis Advisor

Garth V. Hobson
Second Reader

Anthony J. Healey
Chairman, Department of Mechanical and Astronautical Engineering

THIS PAGE INTENTIONALLY LEFT BLANK

ABSTRACT

This thesis presents a Computation Fluid Dynamics (CFD) analysis of the aerodynamic performance of circular and elliptical leading edges of compressor blades, with a range of leading edge droop angles. Specifically, simulations were conducted, with a free stream Mach number of 0.65 to quantify the change in pressure distributions and boundary layer momentum thickness in the leading-edge region for a range of incidences on a flat plate with various leading-edge ellipticity ratios, ranging from unity (circular) to 5.5. In addition, the impact of drooping the leading edge was analyzed over a range of incidence angles from zero to 13 degrees. Pressure distributions indicate that elliptical leading edges can eliminate separation bubbles at zero incidence. The results indicated that the minimum loss occurred at an ellipticity ratio of about 3.5 and elliptical leading edges with a droop slightly greater than the average incidence can significantly decreased aerodynamic losses over a wider range of incidences.

THIS PAGE INTENTIONALLY LEFT BLANK

TABLE OF CONTENTS

I. INTRODUCTION 1
- A. OVERVIEW AND BACKGROUND 1
- B. LITERATURE SURVEY 6
  - 1. Previous Studies 6
  - 2. Summary of Literature Survey 12
- C. OBJECTIVES 12
- D. ORGANIZATION 13

II. METHODOLOGY 15
- A. COMPUTATIONAL FLUID DYNAMICS 15
- B. VALIDATION OF CFD-ACE+ 15
- C. MODEL CREATION 17
  - 1. Ellipticity and Droop 17
  - 2. Blending of the Leading Edge 19
- D. SIMULATION CONDITIONS 26

III. RESULTS AND DISCUSSION 29
- A. RESULTS 29
  - 1. Pressure Distribution 29
  - 2. Boundary Layer Momentum Thickness 35
- B. DISCUSSION OF FLOW FIELDS 42

IV. CONCLUSIONS AND RECOMMENDATIONS 47

APPENDIX A. FLOW SEPARATION 49

APPENDIX B. TABULATED CALCULATIONS 53

APPENDIX C. PRESSURE DISTRIBUTION PLOTS 57

APPENDIX D. MATLAB CODE 65
- A. LEADING-EDGE BLENDING CODE 65
- B. ELLIPTIC CALCULATIONS CODE 68

APPENDIX E. SUPPLEMENTAL FIGURES 71

LIST OF REFERENCES 73

INITIAL DISTRIBUTION LIST 75

THIS PAGE INTENTIONALLY LEFT BLANK

LIST OF FIGURES

Figure 1. NACA 65-213 Airfoil Section 1
Figure 2. Circular Leading Edge of a NACA 0012 Airfoil (see Ref. 23) 2
Figure 3. Attached Boundary Layer Velocity Profile 3
Figure 4. Separated Boundary Layer Velocity Profile 3
Figure 5. Comparison of Elliptic and Circular Leading Edges Attached to a Flat Plate 5
Figure 6. Comparison of Straight Elliptic Leading Edge and Elliptic Leading Edge with a Droop Angle δ 6
Figure 7. Walraevens-Cumpsty Pressure Coefficient ($-C_P$) as a Function of Distance Along the Plate From the Geometric Leading Edge 7
Figure 8. Comparison of Walraevens-Cumpsty and CFD Pressure Coefficients ($-C_P$) for a Flat Plate with Leading-Edge Ellipticity Ratio of 1.89 16
Figure 9. Flat Plate Models with Leading Edges of Varying Ellipticity Ratio 17
Figure 10. Flat Plate Models with Varying Droop Angles of 0, 3.33, 6.66, 10.0, and 13.3 degrees 18
Figure 11. Drooped Leading Edge Before Blending 20
Figure 12. Variation of Radius of Curvature with Arclength From Geometric Leading Edge to Blend Point at Semiminor Apex 21
Figure 13. Radius of Curvature for Pressure Side Blending Region of Drooped Elliptic Leading-Edge Attached to a Flat Plate 22
Figure 14. Comparison of Original Leading-Edge Transition to Blended Leading-Edge Transition on Pressure Side of Plate 23
Figure 15. Final Blade After Blending of Leading Edge on Pressure and Suction Sides 23
Figure 16. Sample Grid Generated in CFD-GEOM Used For Simulations 25
Figure 17. Close-up of Grid At Leading Edge 26
Figure 18. Pressure Distribution ($-C_P$) Over Circular Leading-Edge Model at Various Angles of Attack with Blendpoint Shown 30
Figure 19. Pressure Distribution ($-C_P$) Over All Ellipticities with Zero Droop at Zero Degrees Incidence with Blendpoints Shown 31
Figure 20. Pressure Distribution ($-C_P$) Over Model with an Ellipticity Ratio of 2.5 with No Droop at Various Angles of Attack with Blendpoint Shown 32
Figure 21. Pressure Distribution ($-C_P$) Over Model with an Ellipticity Ratio of 5.5 and Ten Degrees Droop at Various Angles of Attack 33
Figure 22. Pressure Distribution ($-C_P$) Over Model with and Ellipticity Ratio of Four and Various Droop Angles at Six Degrees Angle of Attack 34
Figure 23. Velocity Profiles on the Suction Side (ss) and Pressure Side (ps) of a Plate as Used in the Calculation of the Boundary Layer Momentum Thickness, $\theta_{ss} + \theta_{ps}$ 35
Figure 24. Circular Leading-Edge Boundary Layer Momentum Thickness, $\theta_{ss} + \theta_{ps}$, at Various Angles of Attack 36

Figure 25. Momentum Thickness, $\theta_{ss}+\theta_{ps}$, at the End of the Plate for Various Ellipticity Models....37
Figure 26. Boundary Layer Momentum Thickness, $\theta_{ss}+\theta_{ps}$, for All Ellipticities at Various Angles of Attack and Zero Degrees Droop....38
Figure 27. Boundary Layer Momentum Thickness, $\theta_{ss}+\theta_{ps}$, for Model with Leading-Edge Ellipticity Ratio of 2.5 and All Droop Angles at Various Angles of Attack....39
Figure 28. Boundary Layer Momentum Thickness, $\theta_{ss}+\theta_{ps}$, for Model with Ellipticity Ratio of Four and All Droop Angles at Various Angles of Attack....40
Figure 29. Boundary Layer Momentum Thickness, $\theta_{ss}+\theta_{ps}$, for Model With Ellipticity Ratio of 5.5 and All Droop Angles at Various Angles of Attack....41
Figure 30. Boundary Layer Momentum Thickness, $\theta_{ss}+\theta_{ps}$, for Models of All Ellipticity Ratios with 6.6 Degrees Droop at Various Angles of Attack....42
Figure 31. Leading-Edge Suction Side Separation Bubble....43
Figure 32. Leading-Edge Pressure Side Separation Bubble....43
Figure 33. Leading-Edge View of Blade Model with Ellipticity Ratio of 4, Zero Degrees Droop, Ten Degrees Incidence....44
Figure 34. Leading-Edge View of Blade Model with Ellipticity Ratio of 4, Ten Degrees Droop, Zero Degrees Incidence....45
Figure 35. Pressure Coefficient ($-C_P$) over Model from Geometric Leading Edge with Ellipticity Ratio of 2.5 and Droop Angle of 3.33 degrees....57
Figure 36. Pressure Coefficient ($-C_P$) over Model from Geometric Leading Edge with Ellipticity Ratio of 2.5 and Droop Angle of 6.66 degrees....58
Figure 37. Pressure Coefficient ($-C_P$) over Model from Geometric Leading Edge with Ellipticity Ratio of 2.5 and Droop Angle of 10.0 degrees....58
Figure 38. Pressure Coefficient ($-C_P$) over Model from Geometric Leading Edge with Ellipticity Ratio of 2.5 and Droop Angle of 13.33 degrees....59
Figure 39. Pressure Coefficient ($-C_P$) over Model from Geometric Leading Edge with Ellipticity Ratio of 4.0 and Droop Angle of 0.0 degrees....59
Figure 40. Pressure Coefficient ($-C_P$) over Model from Geometric Leading Edge with Ellipticity Ratio of 4.0 and Droop Angle of 3.33 degrees....60
Figure 41. Pressure Coefficient ($-C_P$) over Model from Geometric Leading Edge with Ellipticity Ratio of 4.0 and Droop Angle of 6.66 degrees....60
Figure 42. Pressure Coefficient ($-C_P$) over Model from Geometric Leading Edge with Ellipticity Ratio of 4.0 and Droop Angle of 10.0 degrees....61
Figure 43. Pressure Coefficient ($-C_P$) over Model from Geometric Leading Edge with Ellipticity Ratio of 4.0 and Droop Angle of 13.33 degrees....61
Figure 44. Pressure Coefficient ($-C_P$) over Model from Geometric Leading Edge with Ellipticity Ratio of 5.5 and Droop Angle of 0.0 degrees....62
Figure 45. Pressure Coefficient ($-C_P$) over Model from Geometric Leading Edge with Ellipticity Ratio of 5.5 and Droop Angle of 3.33 degrees....62

Figure 46. Pressure Coefficient ($-C_P$) over Model from Geometric Leading Edge with Ellipticity Ratio of 5.5 and Droop Angle of 6.66 degrees 63
Figure 47. Pressure Coefficient ($-C_P$) over Model from Geometric Leading Edge with Ellipticity Ratio of 5.5 and Droop Angle of 10.0 degrees 63
Figure 48. Pressure Coefficient ($-C_P$) over Model from Geometric Leading Edge with Ellipticity Ratio of 5.5 and Droop Angle of 13.3 degrees 64
Figure 49. Variation of Elliptical Arclength with Ellipticity Ratio.....71

THIS PAGE INTENTIONALLY LEFT BLANK

LIST OF TABLES

Table 1. Conditions For Walraevens-Cumpsty Test 16
Table 2. Model Ellipticity Ratios and Droop Angles 24
Table 3. Simulation Test Conditions 27
Table 4. Simulation Component Velocities 27
Table 5. Simulation Matrix Indicating Separated Flows Schemes 49
Table 6. Boundary Layer Momentum Thicknesses 53

THIS PAGE INTENTIONALLY LEFT BLANK

LIST OF SYMBOLS

SYMBOL	DEFINITION	Units or Dimensions
a	Semimajor axis	m
b	Semiminor axis	m
C	Circumference	m
$C_P = \frac{P - P_\infty}{\frac{1}{2}\rho U^2}$	Pressure Coefficient	[1]
d	Diameter	m
LE	Leading Edge	
Ma	Mach Number	[1]
P	Static Pressure	Pa
ps	Pressure Side	
P_T	Total Pressure	Pa
R	Gas Constant	$J/kg*K$
r	Radius	m
Re	Reynolds Number	[1]
s	Distance Along Blade Surface	m
ss	Suction Side	
t	Thickness	m
T	Static Temperature	K
u	Local u-component velocity	m/s
U	Reference U-component Velocity	m/s

v	Local v-component Velocity	m/s
V	Reference V-component Velocity	m/s
x	Blade Chordwise Distance	m
α	Angle of Attack	degrees
δ	Droop Angle	degrees
γ	Adiabatic Gas Constant	[1]
ρ	Density	kg/m^3
$\theta = \int_0^\infty \frac{u}{U_\infty}\left(1-\frac{u}{U_\infty}\right)dy$	Momentum Thickness	m
$\upsilon = \frac{\mu}{\rho}$	Kinematic Viscosity	m^2/s

ACKNOWLEDGMENTS

The author would like to thank Professor Knox Millsaps for his help throughout the project for his detailed explanations of fluid dynamics, insights into technical writing, as well as for funding necessary training. Also, Professor Garth Hobson is thanked for his help with the Computational Fluid Dynamics program CFD-ACE+, and for being the second reader.

THIS PAGE INTENTIONALLY LEFT BLANK

I. INTRODUCTION

A. OVERVIEW AND BACKGROUND

The United States Navy depends heavily on the use of gas powered turbine engines for power and propulsion for most of it marine and aviation platforms. However, with the increasing cost of fossil fuels, and the ever present threat of tightening defense budgets, there is an increasing focus on making these power plants more efficient. To date, thousands of studies have been conducted with the aim of increasing the overall efficiency of gas turbines, and, more specifically to increase the efficiency of the turbine's compressor. Methods of reducing losses have been analyzed through the intense study of the aerodynamics of the compressor's blades. In addition to the military, industries in the civilian sector stand to benefit from an increase in overall gas turbine efficiency.

One way to influence the efficiency of the compressor is to modify the geometry of its blades and hence their aerodynamic characteristics. In the 1950's and 1960's, the NACA 65 series blade became popular for use in axial compressors as an innovative and more efficient blade type. Figure 1 is a cross-section of a NACA 65-213 airfoil.

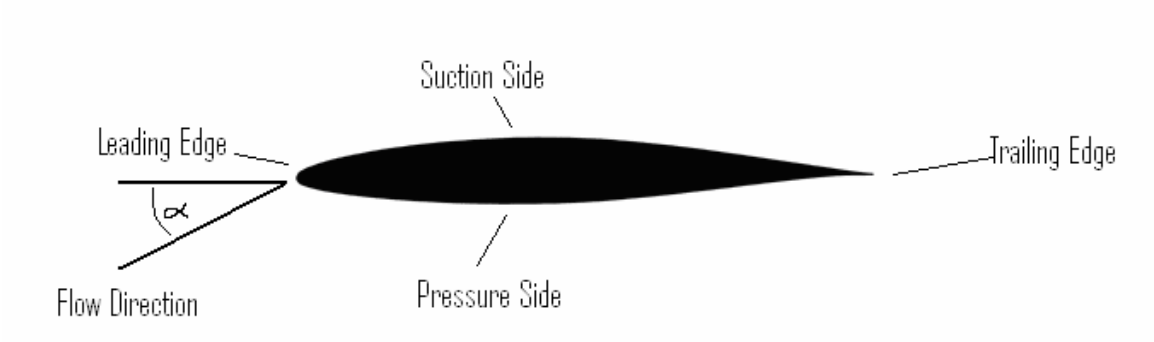

Figure 1. NACA 65-213 Airfoil Section

The geometry of any airfoil can be broken down into three main parts. They are the leading edge shown on the left end of Figure 1, the trailing edge shown on the right end, and the body of the airfoil connecting the leading and trailing edges. The lifting side, shown as the top in Figure 1, is referred to as the suction side, and the bottom side is known as the pressure side.

The most important parts of compressor blade geometry are the leading edge and the trailing edge. The camber and thickness distributions of the body are important, but as long as it smoothly connects the leading and trailing edges, its geometry has secondary impacts on the flow when compared to the leading-edge direction and shape and trailing edge direction.

Today, many gas turbines use a circular shaped leading edge, as can be found on the LM2500 gas turbine, for example. The circular leading edge shape is popular because it is easy to manufacture, and maintains its shape relatively well in the hostile environments encountered. Figure 2 is a close up view of the nose of the NACA 0012 airfoil, which has a circular shaped leading edge.

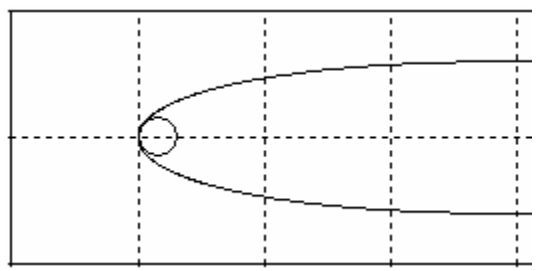

Figure 2. Circular Leading Edge of a NACA 0012 Airfoil (see Ref. 23)

Air flowing around the leading edge of the blade plays an important role in determining the aerodynamic characteristics of the flow over the rest of the blade. As the air approaches the leading edge of the blade, it stagnates, and from there accelerates around the blade, going over either the suction side or the pressure side. The accelerated flow then may or may not undergo a rapid deceleration, depending on the current incidence and other flow factors. If the geometry of the leading edge and the flow conditions result in a large enough deceleration, the flow adjacent to the surface of the blade may experience such an adverse pressure gradient that it actually travels backwards. Figure 3 depicts the velocity vectors of an attached boundary layer flow, whereas the diagram in Figure 4 shows flow that has separated.

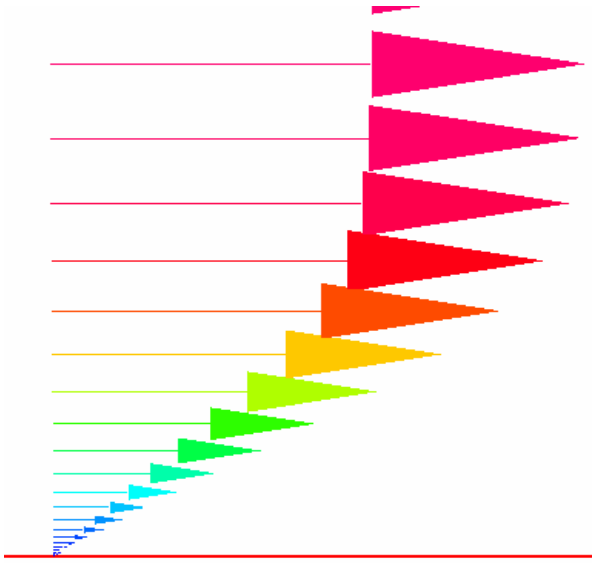

Figure 3. Attached Boundary Layer Velocity Profile

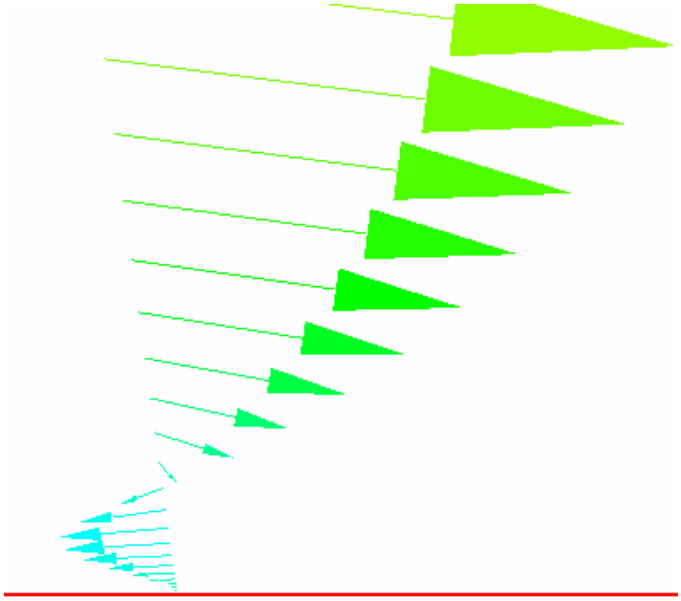

Figure 4. Separated Boundary Layer Velocity Profile 75

If separation occurs, the flow can either reattach along the surface of the blade, or remain unattached. A region where the flow separates and then quickly reattaches is called a separation bubble. The length of these separation bubbles is usually quite small; on average less than five percent of the total chord length. Separation bubbles most

commonly occur very close to the leading edge where the flow undergoes such dramatic acceleration.

The goal of many compressor blade designers has been to create a geometry that will allow the airfoil to operate without the generation of a separation bubble. In cases where the formation of a separation bubble is imminent, mitigating their effects can dramatically improve the overall performance of the blade. However, comparatively little work has been done with a focus on controlling the flow through manipulation of the leading-edge geometry.

One way to decrease the chances of forming a separation bubble on the compressor blade is to redesign the shape and direction of the leading edge. When the flow goes over a circular leading edge, there is very rapid acceleration. However, shapes that allow for the flow to more gradually accelerate and decelerate have been shown to reduce the likelihood of an adverse pressure gradient causing a separation bubble from occurring. The elongated nature of an ellipse has been shown to better control the acceleration and deceleration of the flow around the leading edge.

An ellipse is generally defined as the distance from loci lying on the semimajor axis. The relative distance between the loci is described using an equation relating its semimajor and semiminor axes, and is referred to as eccentricity. The ratio of the semimajor axis to semiminor axis is referred to as the ellipticity ratio. The greater this ratio, the more elongated the ellipse. Figure 5 below depicts a comparison of an elliptic leading edge to a circular leading edge.

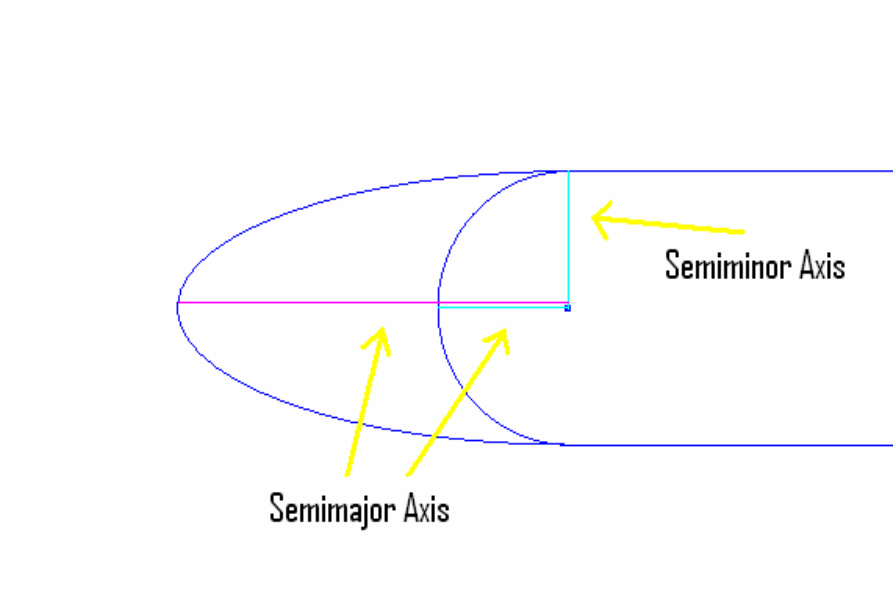

Figure 5. Comparison of Elliptic and Circular Leading Edges Attached to a Flat Plate

In Figure 5, an elliptic leading edge is compared to a circular leading edge, both attached to the same airfoil body. The circular leading edge's semimajor and semiminor axes are the same length, resulting in an ellipticity ratio of unity. The elliptic leading edge has a greater semimajor axis is noticeably less blunt when compared to the circular leading edge. This geometric alteration of the forward section of the blade allows the flow to accelerate and decelerate around the leading edge much more gradually.

In addition to the leading edge shape, the leading edge direction plays an equally important role on impacting the flow and aerodynamic performance of an airfoil. One way researches have observed the impact of the leading-edge direction is by drooping the forward section of the airfoil. The acceleration of the airflow around the leading edge becomes greater with increasing incidence, and drooping the leading edge of the airfoil allows the nose to point more into the oncoming airflow at these higher incidences. In this way, the airfoil can perform as an undrooped leading edge would at lower incidences, and allow the blade to perform better at higher incidences. Figure 6 shows a comparison of a drooped elliptic leading edge to that of a basic elliptic leading edge.

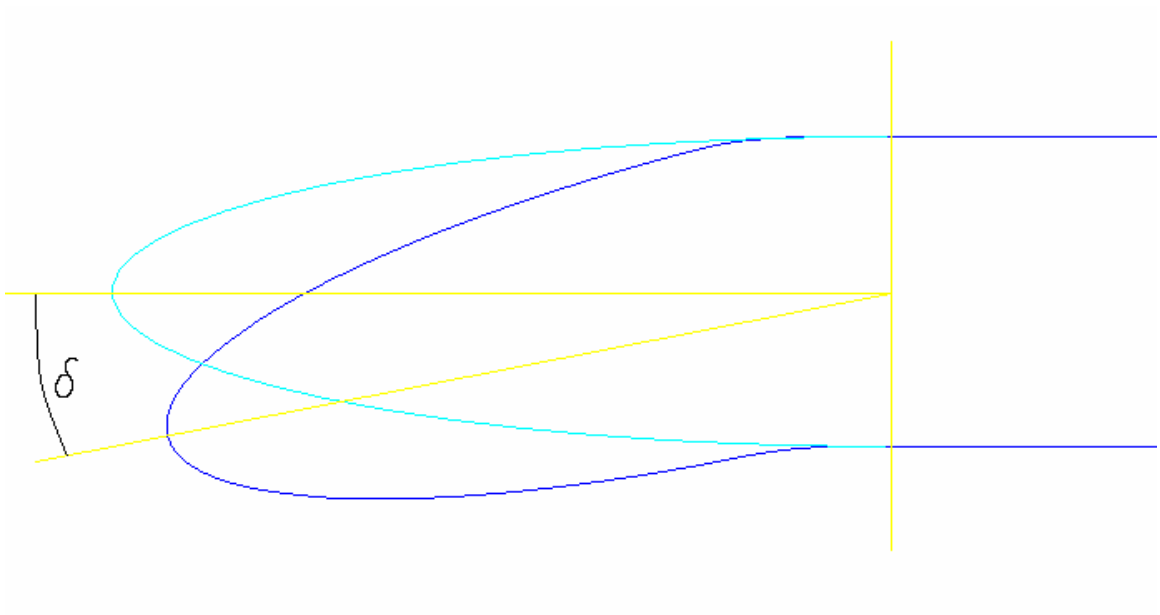

Figure 6. Comparison of Straight Elliptic Leading Edge and Elliptic Leading Edge with a Droop Angle δ

B. LITERATURE SURVEY

Several researches have conducted studies of the impact of leading-edge shape and direction on the aerodynamic characteristics of flow over various airfoils. Their experimental and computational work supports the theory that leading-edge ellipticity and droop can significantly impact pressure distributions and aerodynamic losses.

1. Previous Studies

The experiments of Walraevens and Cumpsty [1] compared the aerodynamic characteristics of a circular leading edge attached to a flat plate to those of a flat plate with a leading-edge ellipticity ratio of 1.89. In their studies, testing conditions were such that the flow remained nearly incompressible. They witnessed that the leading-edge geometry directly affects the aerodynamic performance of the airfoil through its impact on formation of a separation bubble. Figure 7 shows a comparison of the pressure distributions over the two different airfoils.

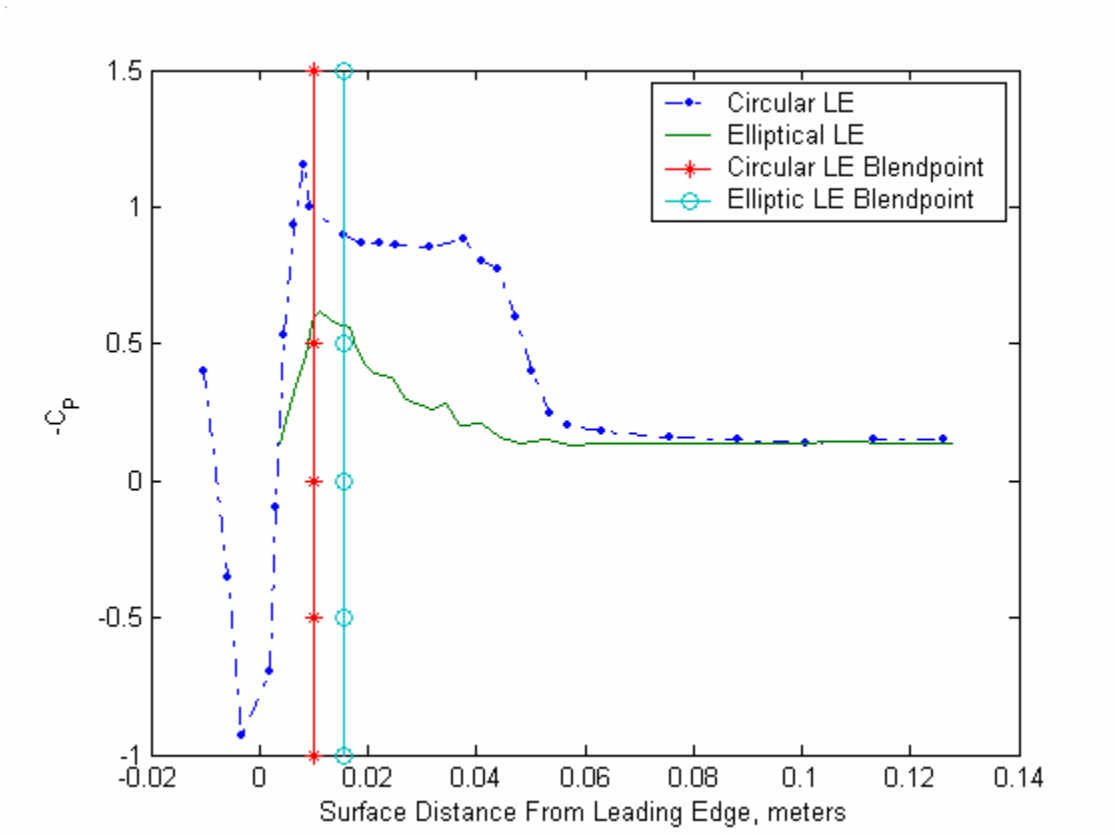

Figure 7. Walraevens-Cumpsty Pressure Coefficient ($-C_P$) as a Function of Distance Along the Plate From the Geometric Leading Edge

Their investigation revealed that for the circular leading edge, the pressure spike reached much higher values than it did for the elliptic leading edge. In addition, the pressure plateau is much longer and higher for the circular leading edge. This is, again, because of the greater deceleration that occurs around the circular leading edge, which resulted in the formation of a separation bubble. With an elliptic leading edge, a separation bubble may not develop at zero incidence because separation is avoided entirely. When the bubbles do form, they are usually shorter in length and are able to reattach to the blade surface at a higher incidence than those which formed on the circular leading-edge models. The boundary layer momentum thickness on the circular leading-edge model was significantly larger than that of the elliptic leading edge, and indicates that an elliptic leading edge reduces losses.

Many airfoil sections used in compressors and turbines have discontinuity in curvature of the leading edge [1] at the transition point from leading edge to airfoil body.

At the very front of the blade, the curvature is quite small, and drastically increases at the point where the leading edge joins the body of the blade. Typical compressor blades, such as the NACA 65 series, have a maximum thickness that ranges from roughly three to 12 percent of the chord length, and a leading-edge thickness that is around 0.4 percent of the chord [1]. When compared to the radius of curvature of the leading edge, the radius of the blade body is almost flat. This discontinuity in curvature, such as with the circular leading-edge model, results in a separation bubble forming even at zero incidence.

Huoxing et al. [2] also determined that the leading-edge shape has a large influence on flow characteristics. This affects separation and transition of the flow, as well as the boundary layer properties after the reattachment point. In their experiments, they tested a circular leading-edge profile, as well as a model with a leading-edge ellipticity ratio of 2.5. In tests of their elliptic leading-edge model, the suction peak in the pressure coefficient distribution was much lower, and the flow did not separate even at six degrees angle of attack. They also witnessed that the effect of the leading-edge shape on the pressure side of the blade was rather weak when compared to the influence on the flow over the suction side. Even at low Reynolds numbers, Huoxing et al. [2] found that a separation bubble could form at low incidence on the circular leading-edge model. Comparatively, if a bubble did form on the elliptic leading-edge model, it was shorter, and allowed the flow to reattach at higher incidences than was possible with the circular leading edge. Huoxing et al. [2] define a separation bubble as a region where a strong adverse pressure gradient can cause a laminar boundary layer to separate. However, once the flow is separated, the shear layer becomes highly unstable and can undergo rapid transition to turbulent flow. This turbulent flow in the separation bubble is able to entrain more fluid from surrounding laminar flow and the turbulent shear layer then usually bends back towards the surface of the blade and reattaches as a turbulent boundary layer. Their tests also revealed that the length of the separation bubble, as well as the pressure distribution and boundary layer characteristics downstream of the bubble were strong functions of incidence. As the flow reattached to the surface there was a steep pressure rise. As they increased testing angle of attack, the formation of the bubble occurred at the same chord-wise point, however the bubble became longer and the level of uniformity in the pressure plateau became lower.

Chandrasekhara et al. [3] performed experiments on a VR-12 helicopter rotor blade during which they statically and dynamically drooped the first 25 percent of the airfoil from zero degrees up through 20 degrees. Their experiments were performed at relatively low Mach numbers, from 0.1 to 0.4. The droop angle is denoted as δ. They discovered that drooping the leading edge allowed for better control of the flow around the nose. When they compared the pressure distribution over the drooped airfoil to that of the undrooped airfoil, the pressure peak was dramatically different. On the undrooped blade, the pressure coefficient peaked out at -7.92, where as on one of their statically drooped models, it only reached -3.46 for the same testing conditions. Also, their study determined that the suction side pressure values of a drooped leading-edge model appeared to lag the basic airfoil in angle of attack. Additionally, when the leading edge was drooped, the flow remained attached to a point farther down the blade. The research conducted by Chandrasekhara et al. [3] also illustrates the importance of a smooth blend between the drooped leading edge and the rest of the airfoil section. For example, they observed a slight distortion in the pressure distribution near the blend point that resulted from the small backward facing step present where the hinge connected the drooped leading edge to the main body. This motivates special attention to be paid to blending the leading edge to avoid tripping the flow.

The benefits of a drooped leading edge are particularly noticeable at higher angles of attack. Chandrasekhara et al. [3] were able to achieve fully attached leading-edge flow even at 20 degrees angle of attack with a drooped nose. Drooping the leading edge also allows for greater control of the acceleration of the flow, similar to the effects of an elliptic edge when compared to that of a circular leading edge. Their drooped model was able to keep the flow well subsonic when compared to the undrooped model, even at 20 degrees alpha. The peak suction over the basic airfoil rose steeply with angle of attack [3]. The flatter pressure distribution seen with a drooped leading-edge implied that there is still a reasonably high amount of lift produced. Drooping the leading edge was able to largely mitigate compressibility affects, which would enable a better performance to be attained from the same airfoil at higher Mach numbers. Drooping the leading edge also pushes the angle of attack at which the VR-12 airfoil stalls to a higher value than attained

with the undrooped leading edge. The data indicated that a greater operating envelope is attainable with a drooped leading edge.

Tuck and Dostovalova [4] found that drooping the leading edge by sharpening the nose can result in better flow control. In their studies, they changed the shape of the nose to best delay separation of the laminar boundary layer. Park [5] arrived at the same conclusion and asserts that a wedge shaped leading edge can be inexpensively created using casting technology that leaves a relatively thick leading edge. Afterwards, the blade can easily be retouched to create the desired leading-edge shape using milling.

Garzon and Darmafol [6] conducted studies on variations in leading-edge geometry that might arise due to manufacturing inaccuracies. The greatest losses occurred as a result of variations in the first five percent of the blade, illustrating the dramatic effects that the leading-edge shape and direction can have on determining flow characteristics over the rest of the airfoil. Additionally, they observed substantial increases in boundary layer momentum thickness as a result of these geometric variations.

Tuck [7] also performed a study that compared lift results to those listed in Abbott and Von Doenhoff [8], and found that the reattachment of the flow is responsible for the underprediction of the angle of attack for maximum lift by a factor of 0.5 to 0.8. He also asserts that the shape of the leading edge will greatly affect whether or not the flow reattaches. Tuck also found that sharp-edged wings stall very quickly, further illustrating the impact of leading-edge geometry on attaining smooth, attached flow over the airfoil.

Suder et al. [9] found that increasing the thickness and adding roughness to a transonic axial-flow compressor rotor can result in a significant degradation in overall performance. In manufacturing and repairing transonic axial blades, Suder et al. [9] believe that the goal should be to make the leading edge as smooth as possible and so that it will stay that way for as long an operating period as possible. Applying a protective coating to the blade increases resistance to degradation. These coatings do, however, results in an increase of the suction side boundary layer thickness due to their impact on leading-edge geometry.

The unintentional blunting of the leading edge can have detrimental effects on the flow field over an airfoil. Reid and Urasek [10] found that for relatively small compressors, the leading edge of the rotor blades may be blunt due to manufacturing tolerances. For larger blades, the leading edge may become blunt due to foreign object damage or corrosion. In transonic rotors, a blunt leading edge tends to increase the shock losses associated with a detached bow wave system. With a blunt leading edge, the total pressure ratio, total temperature ratio and adiabatic efficiency is much lower than that for the circular leading edge.

Tain and Cumpsty [11] performed experiments and simulations with a circular leading edge attached to a flat airfoil at Mach numbers ranging from 0.6 to 0.95. The extent to which the airflow accelerates around the leading edge is dependent on the shape of the leading edge. They found that you can expect the flow to become sonic around a circular leading edge of an airfoil.

Computational Fluid Dynamics is heavily relied upon as a method of predicting leading-edge flow behavior. Calvert [12] investigated an inviscid-viscous method to modeling leading-edge separation bubbles, and found that they are most likely to occur near the leading edge of sharp-edged blade sections in axial compressors and turbines. This is particularly the case when the blade sections are operated at positive incidence. Calvert [12] also found that the overall performance of the blade section can be significantly affected by the thickness of the initial boundary layer.

Mason [13] asserts that the Navier-Stokes solutions used in computational fluid dynamic studies do not adequately address the flow field solution near the leading edge. His work stresses the importance of leading-edge flow on boundary layer development.

Environmental conditions have been shown to significantly alter the leading-edge shape. Wickens and Nguyen [14] observed leading-edge changes that resulted from ice accretion on a propeller, and found that there was a large loss of lift and an increase in form drag as a result of the modification of the leading edge. Their tests also showed a large dependency on Reynolds number.

Simulations of ice accretion were performed by Kwon and Sankar [15] using a three-dimensional compressible Navier-Stokes solver. Their investigation indicates that

leading-edge separation and reattachment can be caused by changes to the leading-edge shape from ice accretion. Similarly, Broeren et al. [16] confirmed that the separation bubble became larger as the leading-edge shape became increasingly non-uniform as a result of ice accretion.

Lu and Xu [17] performed an investigation of a circular leading edge with a flat section both experimentally and using CFD. They found that the double suction spikes on the flat edges are much weaker than the single spike that appears with a traditional circular leading edge. At higher incidences, the separation downstream of the leading edge was weaker with the flat. Lu and Xu [17] claim that this improvement in performance was better or equal to that expected with an elliptical leading edge; however they believe that the circular leading edge with a flat is more tolerant to manufacturing inaccuracy than the elliptical shaped leading edge.

2. Summary of Literature Survey

Several researchers have experimentally and numerically investigated the effects of leading-edge geometry modification on flow field properties. They have concluded that ellipticity and droop angle can significantly impact flow separation and transition to turbulence. The combined effects on pressure distribution and aerodynamic losses of a drooped elliptic leading edge at varying incidences have not been extensively studied in the flow conditions present in a typical compressor.

C. OBJECTIVES

The current study focuses on the combined effects of ellipticity ratio and leading-edge droop over a range of incidences on the aerodynamic losses for a compressor blade. It is the overall aim to provide insight into how these geometrical variations impact the flow at a Mach number and Reynolds number typical of those in a compressor. More specifically, the objectives of this thesis are to:

1) Demonstrate ESI-CFD's ability to accurately predict flow behavior when compared to results of previous experimental studies.

2) Obtain numerical results for the pressure distribution over the blade as well as boundary layer momentum thickness at a specified point on the model for simulations performed at typical compressor conditions.

3) Observe the impact of incidence on the flow over models with leading-edge ellipticity and droop.

4) Determine an optimum leading-edge ellipticity ratio and droop angle that provides the greatest reduction in aerodynamic losses.

D. ORGANIZATION

Chapter II presents the methodology used to conduct the research on leading-edge shape and direction. Methods used in model creation are discussed. Also, the steps involved in the CFD simulations, as well as the simulation conditions and variations are explained.

Chapter III provides a graphical representation of the results obtained during the simulations. A discussion is also presented to further explain and identify key results of the study and their significance.

Chapter IV contains conclusions that are drawn based on the results obtained, and a summary of their impact on the study's objectives is also provided.

THIS PAGE INTENTIONALLY LEFT BLANK

II. METHODOLOGY

A. COMPUTATIONAL FLUID DYNAMICS

The research conducted in the current study was performed using Computation Fluid Dynamics. The ESI-CFD program, developed by CFDRC, was chosen for use in the simulations. This code is based on three main parts; a pre-processor, the processor and the post-processor. These subprograms were used to define the model, setup and run the problem, and collect the data that the simulations produced.

The model geometries were created in MATLAB and coordinates for plates and their leading edges were inputted into the pre-processor, CFD-GEOM. In this subprogram, geometrical parameters of the simulation were established such as where the inlet would be in relation to the model. After creating the boundaries of the problem, a grid was be generated which allows the user to discretize the geometry into computational cells.

In the processor, CFD-ACE+, initial, volume, and boundary conditions were applied to the model created in CFD-GEOM. Flow conditions were defined and preferences were set for spatial differencing, iteration limits, as well as relaxation factors. The problem was run from within CFD-ACE+, and allowed the user to observe how well the problem converges.

The post processor, CFD-VIEW, allows the user to visualize and analyze the solution. Surface and line plots were created to retrieve data from within the flow field. The data sought by the user was then taken from the post-processor and reduced in MATLAB.

B. VALIDATION OF CFD-ACE+

To validate the results obtained using the ESI-CFD programs, a comparison study was performed based on the work of Walraevens and Cumpsty [1]. A simulation model was constructed and run at the same conditions as an experiment that they performed on an elliptic leading-edge plate, as outlined in Reference [1]. Table 1 lists the conditions at which the simulation and experiment were run.

Table 1. Conditions For Walraevens-Cumpsty Test

Ellipticity Ratio	1.89
Angle of Attack	0 deg
Velocity	7.2227 m/s
Density	1.1614 kg/m^3
Kinematic Viscosity	1.589E-5 m^2/s
Reference Static Pressure	0.1 MPa

Pressure data were taken around the surface of the model. This was used in obtaining the pressure coefficient. Figure 8 compares the pressure coefficients obtained by Walraevens and Cumpsty to that obtained by CFD.

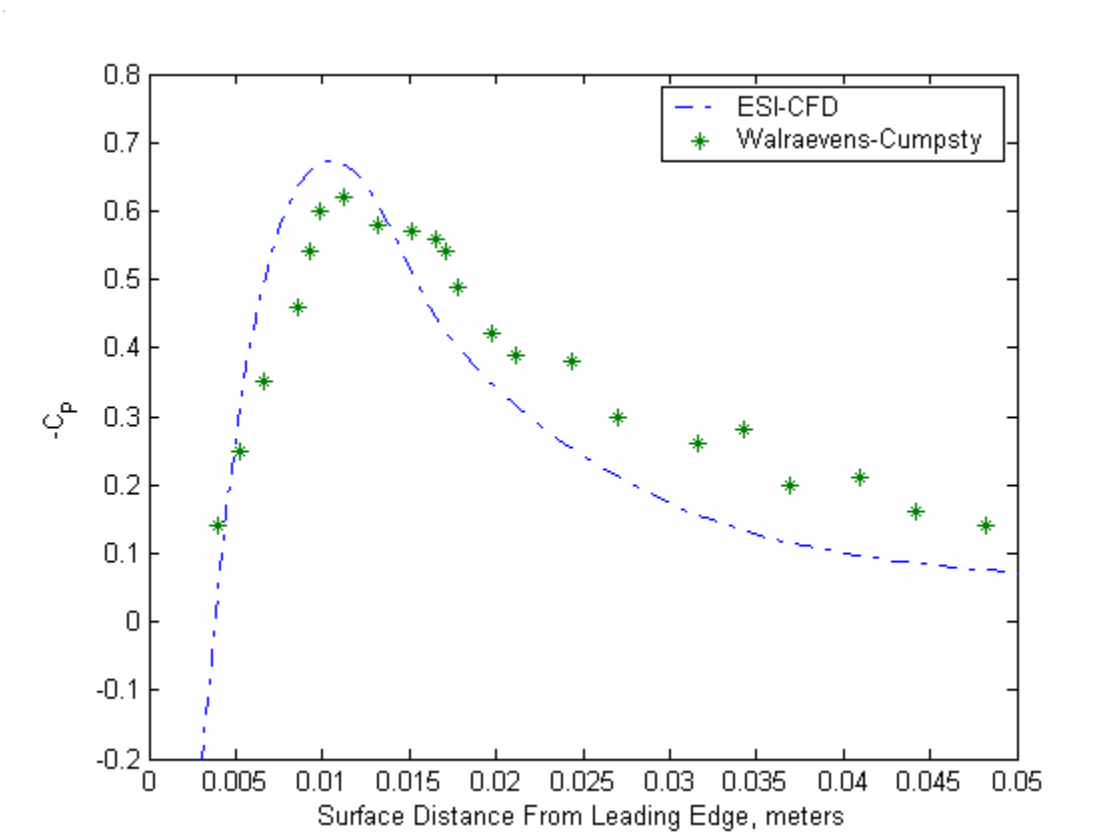

Figure 8. Comparison of Walraevens-Cumpsty and CFD Pressure Coefficients ($-C_P$) for a Flat Plate with Leading-Edge Ellipticity Ratio of 1.89

As Figure 8 shows, the pressure plots do not exactly coincide. The disparity between the two pressure plots lies in the fact that in the experimental setup, Walraevens and Cumpsty used 0.5 percent turbulence; however, in the CFD simulation, no turbulence

was used. However, these results are able to validate the CFD code's prediction ability because the pressure peak has approximately the same value between the simulation and the experiment. Also, the location of the pressure peak along the surface of the plate is almost identical in the experiment and simulation. This suggests that the CFD simulations provide results that are close to, if not the same as, what would be obtained experimentally.

C. MODEL CREATION

1. Ellipticity and Droop

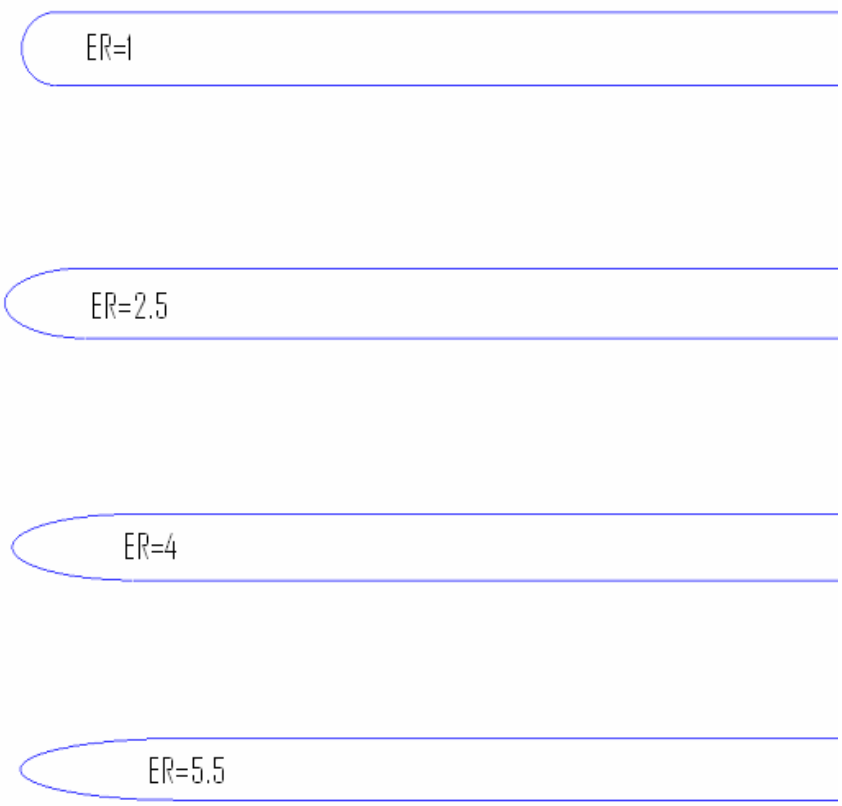

Figure 9. Flat Plate Models with Leading Edges of Varying Ellipticity Ratio

Figure 9 shows the physical impact of varying the ellipticity ratio of the leading edge. The models shown in the figure have, from top to bottom, an ellipticity ratio of 1, 2.5, 4, and 5.5. The calculation of the circumference of the ellipse for the undrooped models was done using Ramanujan's approximation [18]. The equation used was:

$$C \cong \pi\left(3a+3b-\sqrt{(a+3b)(b+3a)}\right) \tag{1}$$

Equation (1) allowed for the determination of the distance along the surface from the geometric leading edge to the blend point of the undrooped models. Figure 49 of Appendix E presents this equation graphically for the undrooped models tested.

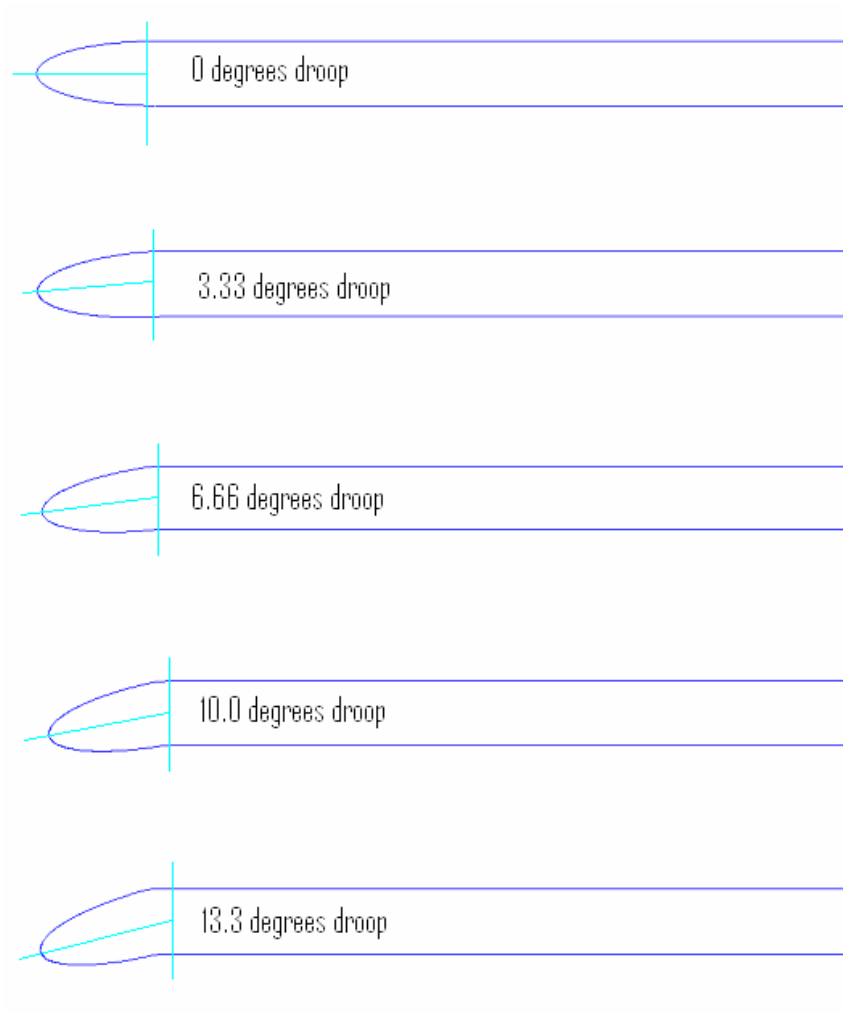

Figure 10. Flat Plate Models with Varying Droop Angles of 0, 3.33, 6.66, 10.0, and 13.3 degrees

The effect of droop is shown in Figure 10. Each blade shown has the same ellipticity ratio; however the droop varies from, top to bottom, 0, 3.3, 6.6, 10, and 13.3 degrees. The droop angle is defined as the angle from the centroid of the ellipse to the apex of the semimajor axis at the leading edge.

Each model was created by taking a flat plate of constant thickness and attaching a different leading edge to it. Although not a full representation of the geometry of an entire compressor blade, using a flat plate as the body still allows for the analysis of the leading edge's effects on the flow characteristics over the model, and what could be expected for a compressor blade. The circular leading-edge model required that a circle of the same diameter as the plate be used, and simply attached as a half circle to the front of the blade model. A similar method was used for the undrooped elliptic leading-edge models. However, for the models where the leading edge was drooped, further modifications were required. The thickness of the plate body is a constant eight millimeters, and the length of the body, without the leading edge, is 0.0945 meters.

2. Blending of the Leading Edge

The drooped leading edges were created by taking an ellipse of specified ellipticity ratio, and rotating it to the desired droop angle. This canted ellipse was then laid over the front of the flat plate. Initially, the excess ellipse and flat plate that remained were "trimmed" away, and a complete airfoil was created.

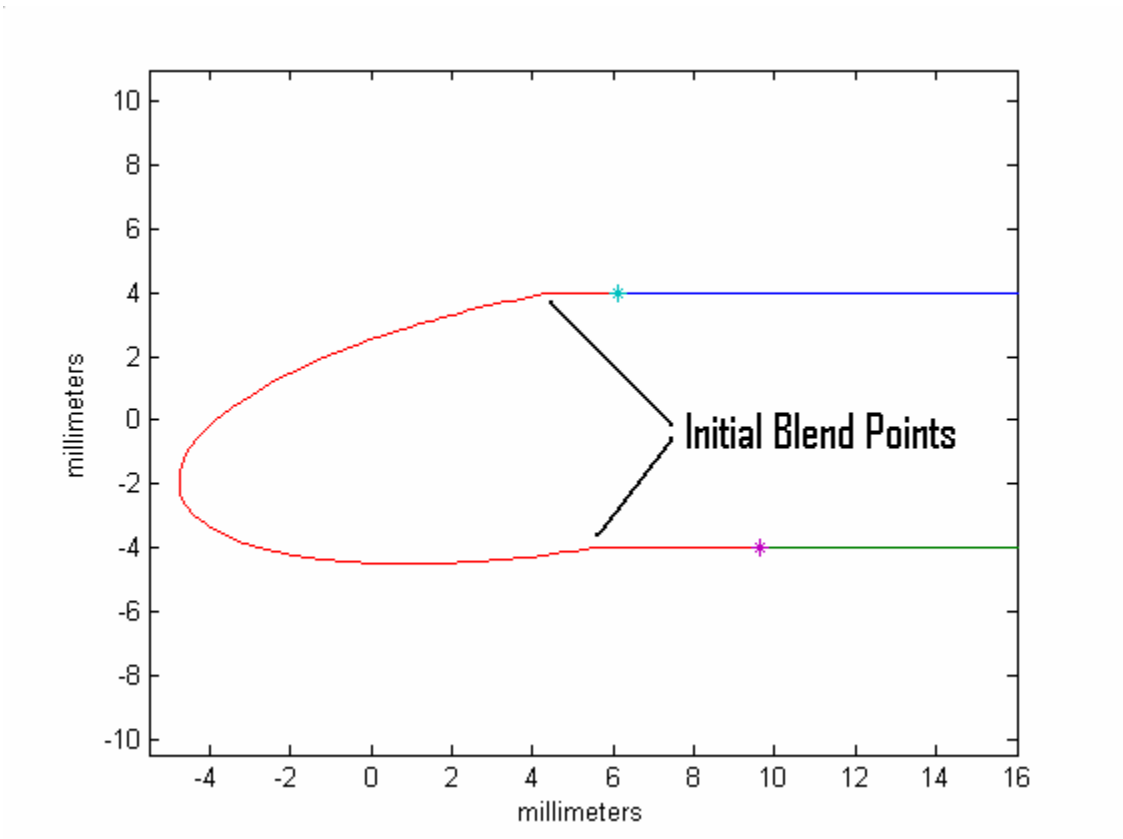

Figure 11. Drooped Leading Edge Before Blending

As Figure 11 shows, the intersection of the drooped, elliptic leading edge and the flat plate can clearly be seen. The resulting combination of the two geometries creates a sharp point on both the suction and pressure sides. These pronounced corners can trip the boundary layer flow, and cause early transition to turbulence or the formation of a separation bubble.

In the design of leading-edge shapes, a very important element to take into account is the radius of curvature of the leading edge, as well as how it changes from the leading edge towards the body. A circular leading edge has a well defined, constant radius. At the point where the circular leading edge is mated with the airfoil body, there is a very large increase in radius of curvature. This dramatic change in curvature has been found to cause separation. However, with an elliptical leading edge, the rate at which the

radius of curvature changes is not as dramatic. Figure 12 presents a comparison of the radius of curvature at the leading edge and the blend point for leading edges of varying ellipticity ratio.

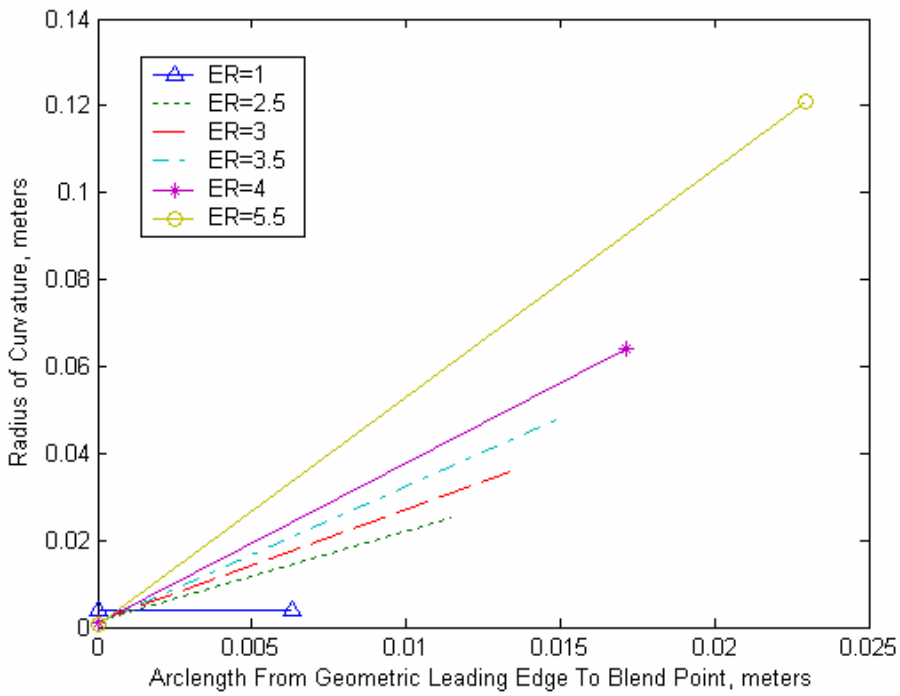

Figure 12. Variation of Radius of Curvature with Arclength From Geometric Leading Edge to Blend Point at Semiminor Apex

At the very front of an elliptic leading edge the radius is small, and gradually increases towards the apex of the semiminor axis. In Figure 11, where there is a sharp corner, a very small radius of curvature exists. In order to allow for a more gradual change in radius of curvature, the sharp corner where the leading edge and blade body are joined was replaced. This was achieved by removing a section of the leading edge and blade body where the two join on both the suction and pressure sides. Around this point, a section of a circular arc was fitted. As a result, a smooth transition is created from the leading edge to the body of the blade, and the likelihood that the transition point between the two would result in early transition to turbulence or a separation bubble is decreased. Figure 13 illustrates the newly fitted transition region from the leading edge to the blade body. The two lines running vertically join at the center of the circular section that was

used to create the transition on the pressure side of the blade, and indicates the typical radius of curvature used for these transition sections.

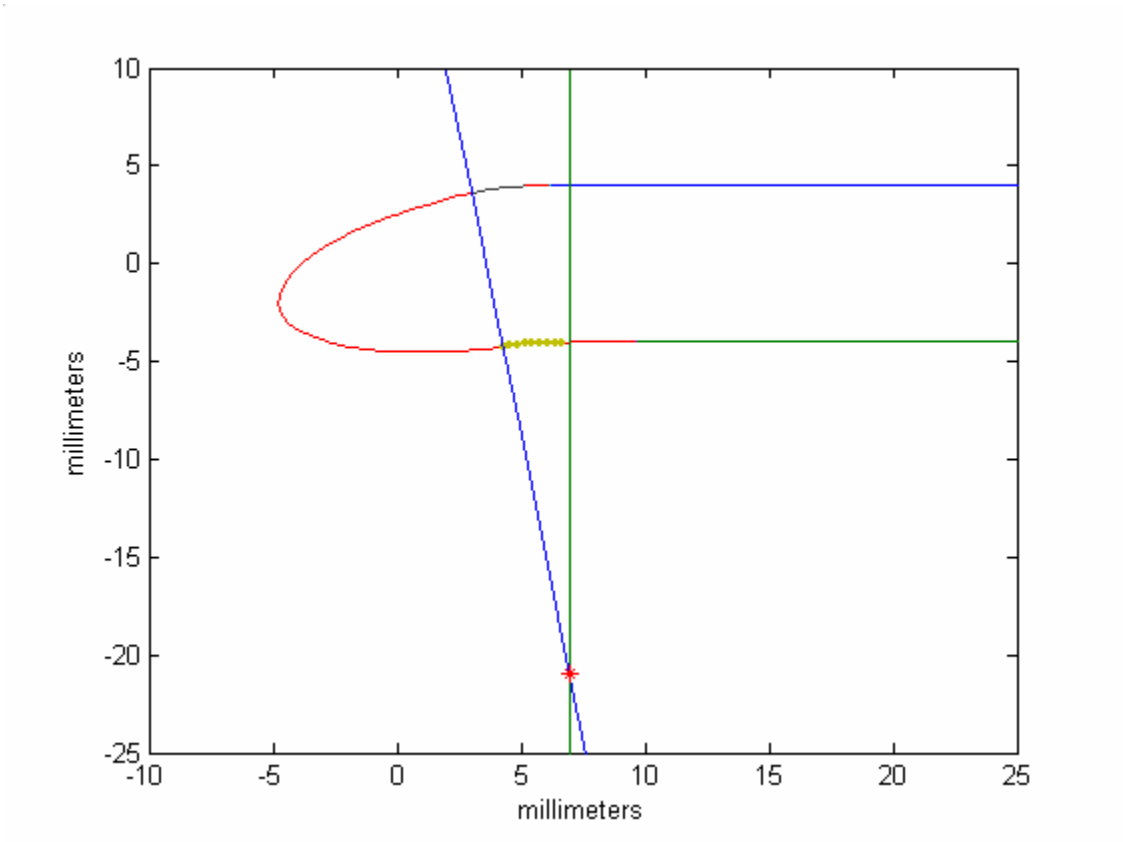

Figure 13. Radius of Curvature for Pressure Side Blending Region of Drooped Elliptic Leading-Edge Attached to a Flat Plate

Figure 14 shows a close-up comparison of the sharp leading edge originally used to the circular arc fitted to the models for a smooth transition. Figure 15 shows an example of a final leading-edge shape that was used after being refitted with a smoother joining region. Instead of the sharp corners that are shown in Figure 11, the leading edge is smoothly mated to the airfoil body. As the droop angle increased, smaller radii of curvature sections were fitted. Also, for the larger ellipticity ratio blades, larger radii of curvature sections were used because of the larger radius of curvature that occurs at the semiminor axis with a larger ellipse.

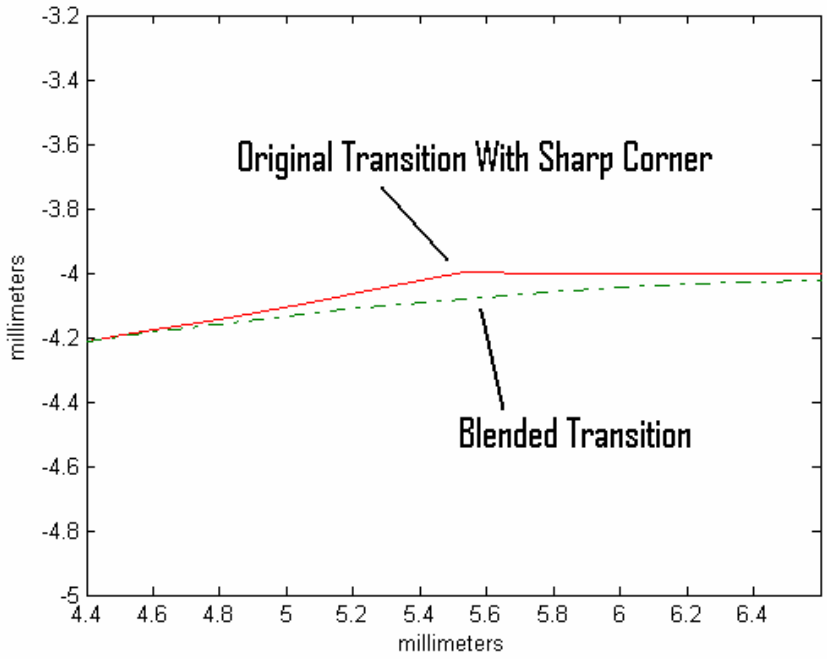

Figure 14. Comparison of Original Leading-Edge Transition to Blended Leading-Edge Transition on Pressure Side of Plate

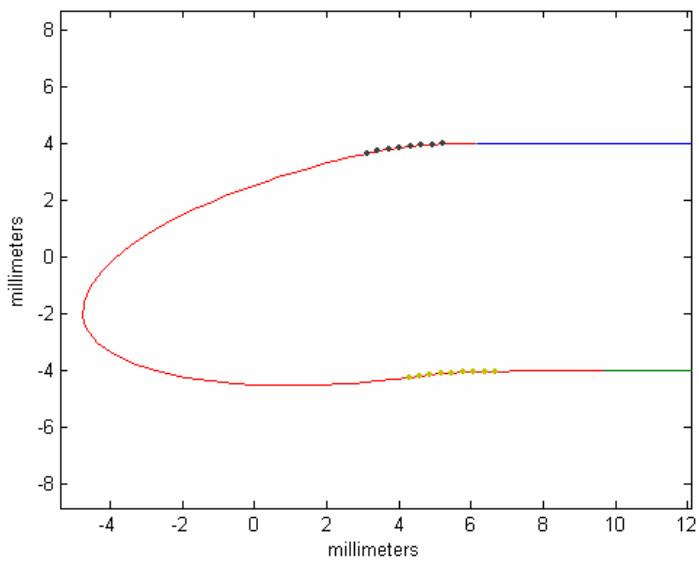

Figure 15. Final Blade After Blending of Leading Edge on Pressure and Suction Sides

The schematic in Figure 15 depicts the final product for a leading edge with an ellipticity ratio of 2.5 and a droop angle of 13.3 degrees. The transition regions on both the suction and pressure side are blended to allow for the smooth flow from the leading edge to the plate body.

Table 2 lists the leading-edge geometric variations that were studied. Ellipticity ratios were first chosen, ranging in value from less than one to 5.5. Performing simulations on a blade model with an ellipticity ratio of less than one allows for the effects of a blunt leading edge to be observed. Past theory holds that an ellipticity ratio of four is optimum for the minimization of losses. Therefore, models with an ellipticity ratio lower and higher than this were tested to determine if an ellipticity ratio of four is indeed optimal.

Table 2. Model Ellipticity Ratios and Droop Angles

Ellipticity Ratio	**Droop Angle (degrees)**
1	0.0
2.5	0.0
2.5	3.33
2.5	6.66
2.5	10.0
2.5	13.3
3	0.0
3.5	0.0
4	0.0
4	3.33
4	6.66
4	10.0
4	13.3
5.5	0.0
5.5	3.33
5.5	6.66
5.5	10.0
5.5	13.3

After the geometry of the models to be used had been set, simulation models had to be constructed using the pre-processor, CFD-GEOM. 'Tab' files were made to input the model geometry data into this subprogram. Edges and surfaces were defined, and a grid was constructed based on the basic plate and leading-edge geometry.

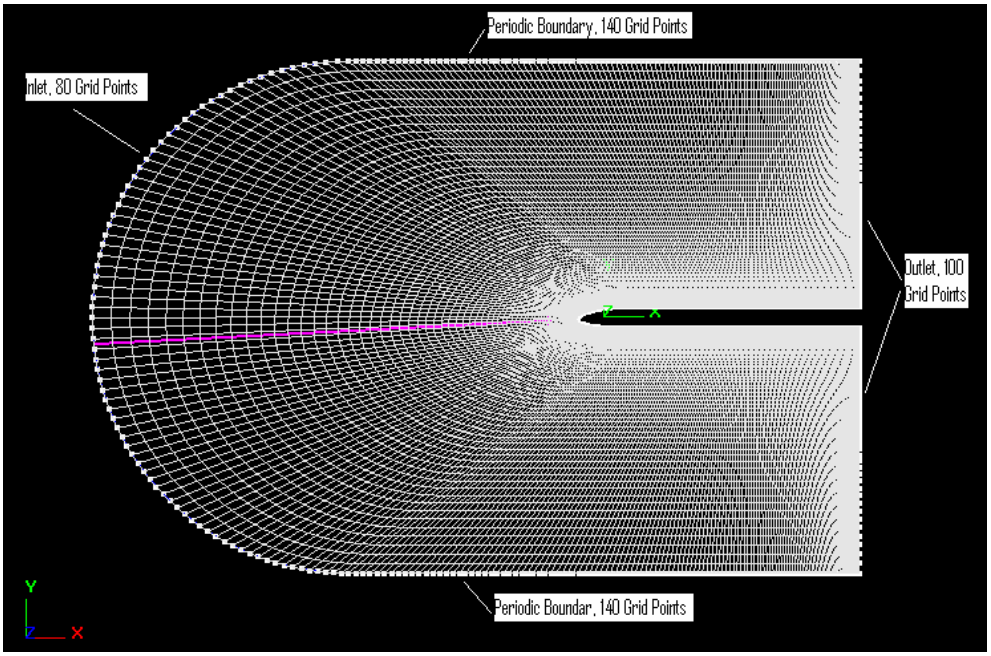

Figure 16. Sample Grid Generated in CFD-GEOM Used For Simulations

Figure 16 represents a typical grid used to define the simulation space about the plate and leading edge. Despite a variation in overall blade length due to different ellipticity ratios, the grid size remained constant. The overall height and length of the grid are 0.2 meters and 0.2995 respectively. The inlet region is semicircular, and was designed this way so that the grid contours would more closely match the general leading-edge shape. On both the suction side and pressure side of the plate, 140 grid points were used, and 80 grid points placed were placed along the leading edge. Blade length was held at a constant 0.0945 meters between the different models, and the length of the leading edge was varied according to the specified ellipticity ratio. Defining the boundaries with the number of grid points specified in Figure 16 resulted in 35,800 nodes used for simulations.

Figure 17 provides a close up view of the grid at the leading edge of a model. The grid becomes much denser close to the surface of the blade, increasing with a power law factor of four. Grid refinement was necessary close to the blade surface to allow to high spatial resolution within the boundary layer. To ensure that a sufficient number of grid points would exist within the boundary layer, the boundary layer momentum thickness was calculated for a flat plate of the same length as the blade body. At the point where

boundary layer momentum thickness was to measured, a minimum of ten grid points were contained within the boundary layer for all cases.

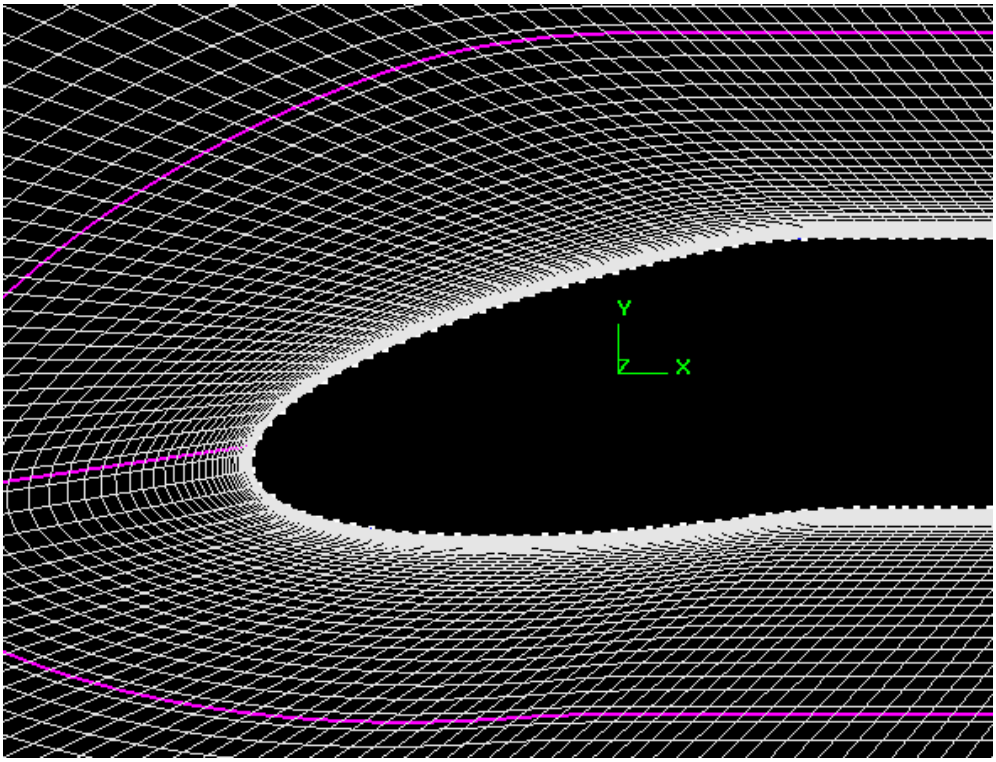

Figure 17. Close-up of Grid At Leading Edge

A grid dependency study was conducted to determine the impact of the grid resolution used for the simulations. This was performed by doubling the number of grid points on each boundary and comparing results for boundary layer momentum thickness. Although the answers between the two grids were different, their disparity was less than a few percent, validating the original grid's ability to produce reliable results without the dramatic increase in computation time.

D. SIMULATION CONDITIONS

Before simulation runs could be made using CFD-ACE+, the problem had to be properly set up with defined boundary conditions, volume conditions, and solver conditions. Table 3 lists the conditions that were inputted into CFD-ACE+. A plate length Reynolds number of about 1.4 million was determined according to the equation

$$\mathrm{Re} = \frac{Ux}{\upsilon} \tag{2}$$

A Mach number of 0.65 is typical of core compressor conditions. The Mach number was arrived at according to equation (3)

$$Ma = \frac{U_\infty}{\sqrt{\gamma RT}} \tag{3}$$

The kinematic viscosity listed was held constant for all simulations. Boundary conditions were defined for the inlet and outlet. The top and bottom boundaries in Figure 12 were set to be periodic. This allowed the solution for the simulation of one blade to represent what could be expected for a cascade of compressor blades. The inlet condition was set according to the velocities listed in Table 4, to impact the specified incidence on the model. The initial condition was set to be close to the inlet velocity to allow for faster convergence. Central spatial differencing was used with a blending factor of 0.1. Relaxations were set to 2 for velocities and 0.1 for pressure. A convergence criterion was set to 0.00001. All blade models were run at incidences of 0, 3, 6, 10 and 13 degrees.

Table 3. Simulation Test Conditions

Temperature	293 K
Density	1.2047 kg/m^3
Kinematic Viscosity	1.508E-5 m^2/s
Reference Static Pressure	101325 Pa

Table 4. Simulation Component Velocities

Incidence (deg)	U-Component Velocity (m/s)	V-Component Velocity (m/s)
0	223.02	0
3	222.72	11.67
6	221.80	23.31
10	219.64	38.73
13	217.31	50.17

THIS PAGE INTENTIONALLY LEFT BLANK

III. RESULTS AND DISCUSSION

A. RESULTS

1. Pressure Distribution

The pressure coefficient was determined for each run by taking pressure data around the surface of the blade, and reduced using the equation (4)

$$C_P = \frac{P - P_\infty}{\frac{1}{2}\rho U^2} \tag{4}$$

This equation is most commonly used for low speed, incompressible flows. The denominator of equation (4) is often represented by the difference between the total and static pressure, P_{T1}-P, which is approximately equal to the dynamic head for low Mach number flows. However, because this study used a consistent free stream Mach number of 0.65, this equation provides very close answers even in the compressible flow region.

A compilation of pressure distributions is included in this section. It is a selection of figures that represent the general behavior of the pressure coefficient over the models. Plots for each individual model can be found in Appendix C. The figures shown represent the pressure coefficient near the leading edge of the blade, where the flow characteristics have a significant effect on the flow over the rest of the blade. Measurements are based on the distance from the nose of the leading edge.

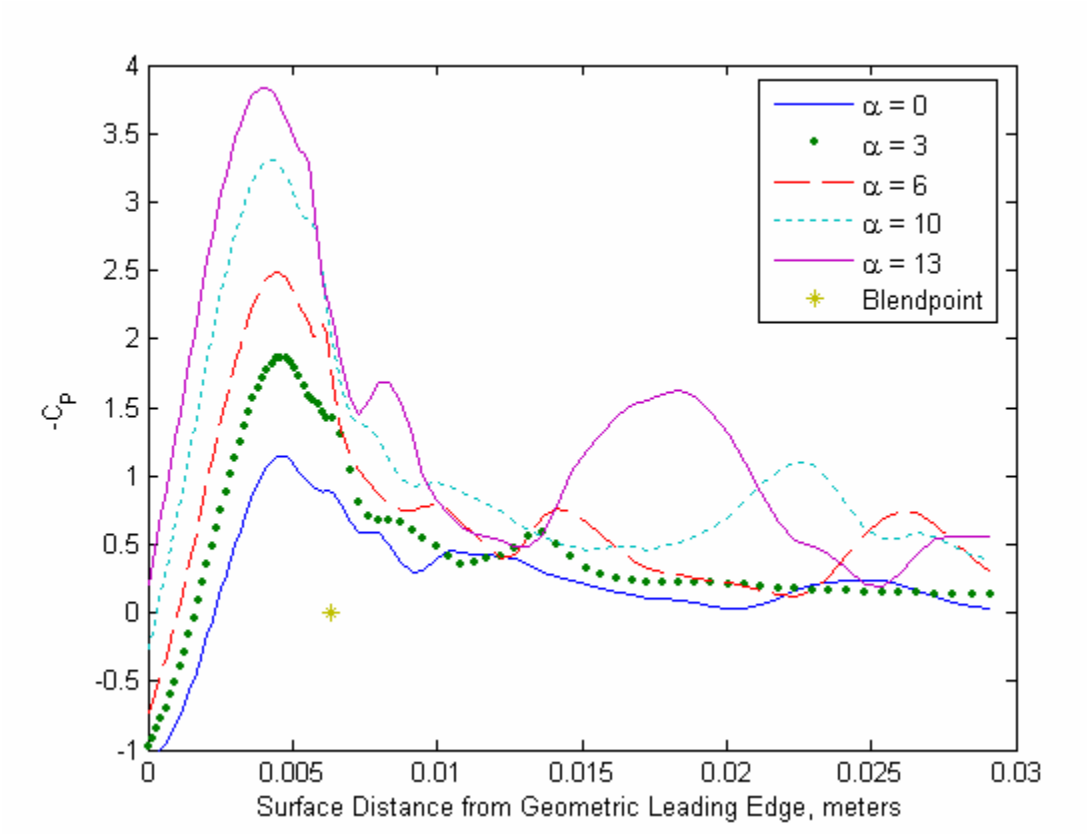

Figure 18. Pressure Distribution ($-C_P$) Over Circular Leading-Edge Model at Various Angles of Attack with Blendpoint Shown

One of the goals of this study was to determine a leading-edge geometry that provided a better pressure distribution over the blade. It was therefore necessary to analyze the pressure distribution over a model with a circular leading edge, such as is presented in Figure 18. The figure shows that as the angle of attack increases, the height of the pressure spike increases, and the flow farther downstream of the leading edge becomes increasingly poorly behaved. If the plate were infinitely long, the pressure coefficient should eventually go to zero. Also, from the line representing the pressure distribution at zero degrees angle of attack, obvious perturbations in the pressure coefficient can be seen. This indicates a strong adverse pressure gradient exists on the circular leading edge, and that the flow may be separating even at zero incidence. Visualizations of the flow from the post-processor confirmed this, as well as the results obtained by Walraevens and Cumpsty [1] in their experiments using a circular leading edge attached to a flat plate.

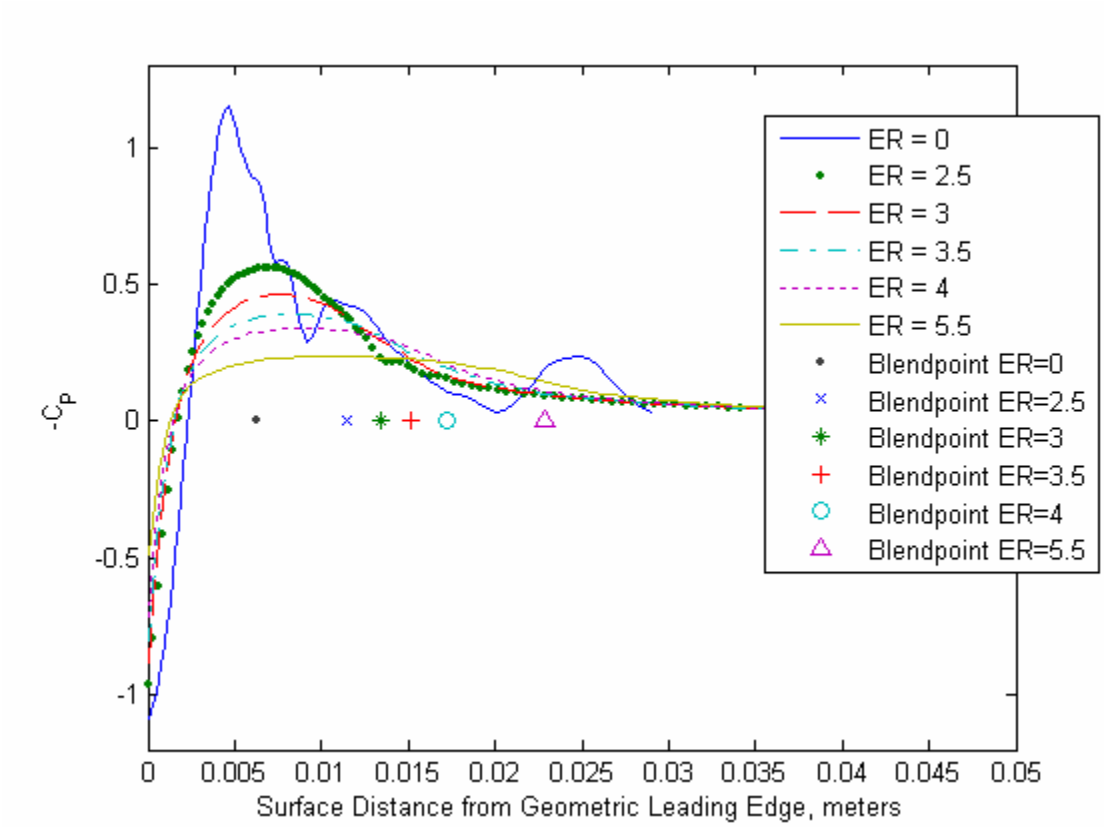

Figure 19. Pressure Distribution ($-C_P$) Over All Ellipticities with Zero Droop at Zero Degrees Incidence with Blendpoints Shown

Figure 19 displays the pressure variations as a function of ellipticity ratio. The important trend to notice in this figure is that the pressure spike decreases its magnitude as the ellipticity ratio increases. Also, the region of pressure elevation becomes much more elongated with the more elliptic leading edges. This is caused by the more gradual acceleration and deceleration of the flow around the leading edge as the ellipticity increases. The backside of the pressure peak is also important, and is a strong indication of whether or not the flow separates. The plateaus that appear on the backside of the pressure peak on the circular leading edge suggest the presence of a separation bubble. Even for the model with an ellipticity ratio of 2.5, a small perturbation and plateau can be seen on the backside of the pressure peak. This indication of flow separation was confirmed with flow visualization in the post-processor. However, for the blade model with an ellipticity ratio of 5.5, for example, the backside of the pressure peak is very smooth, and suggests that the flow remains fully attached to the blade surface and does not separate.

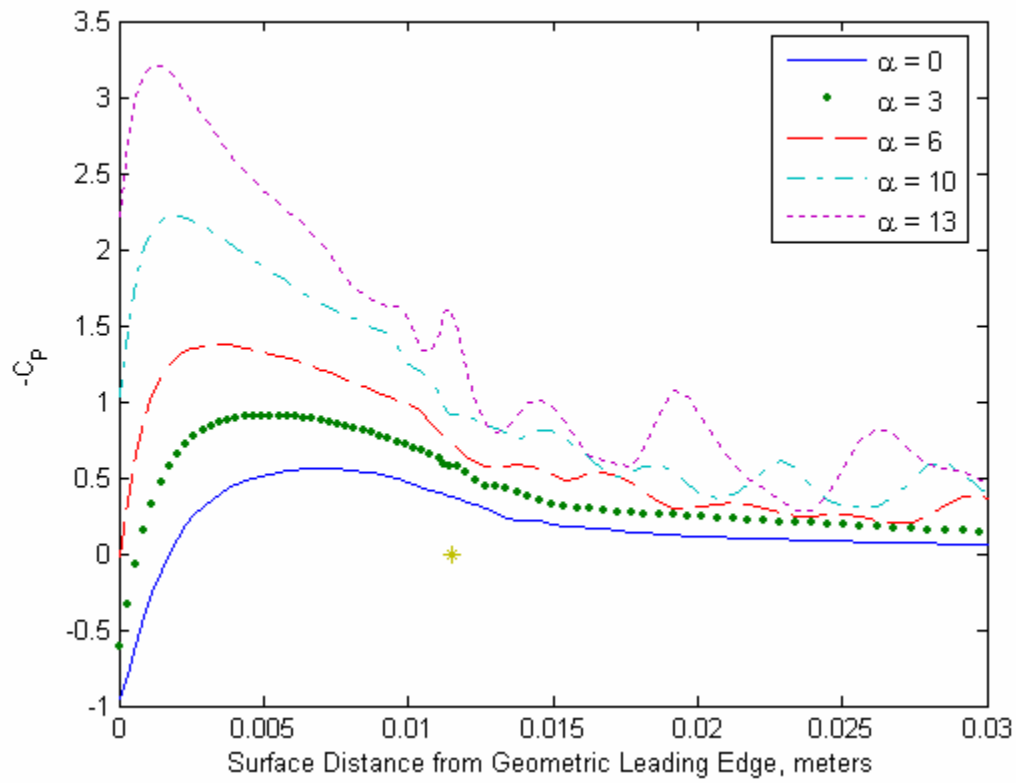

Figure 20. Pressure Distribution ($-C_P$) Over Model with an Ellipticity Ratio of 2.5 with No Droop at Various Angles of Attack with Blendpoint Shown

Observing the impact of ellipticity on pressure distribution, Figure 20 provides insight into the flow behavior for the blade model with an ellipticity ratio of 2.5. Similar to the trend observed in Figure 18 for the circular leading edge model, as the angle of attack increases, the height of the pressure spike increases. Additionally, the flow on the suction side is well behaved at the lower incidences, as indicated by the smooth pressure distribution after the peak pressure point. Despite the fact that at the higher incidences Figure 20 suggests separation, the pressure peak is still significantly lower than it was for the circular leading-edge model. The oscillations after the pressure peak, as shown for the higher incidences, indicate that there are multiple regions of separation on the suction side of the plate.

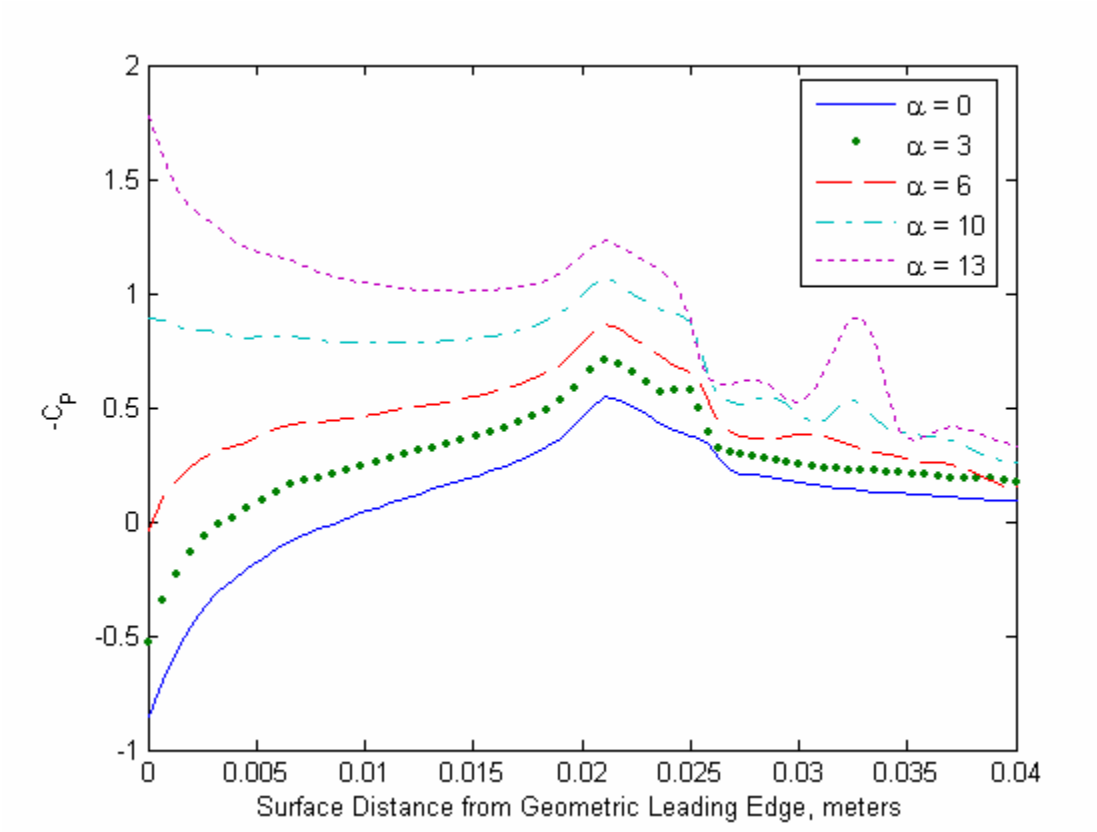

Figure 21. Pressure Distribution ($-C_P$) Over Model with an Ellipticity Ratio of 5.5 and Ten Degrees Droop at Various Angles of Attack

Figure 21 shows the effect of an elliptic leading edge that has ten degrees of droop. The plot represents the pressure distribution from the nose of the leading edge back, and again suggests that the flow is well behaved at lower angles of attack. The bumps in the pressure distribution after the pressure spike at the higher angles of attack indicate that the flow may be separating. However, the magnitude of these pressure fluctuations is still significantly less than it is for the circular leading edge.

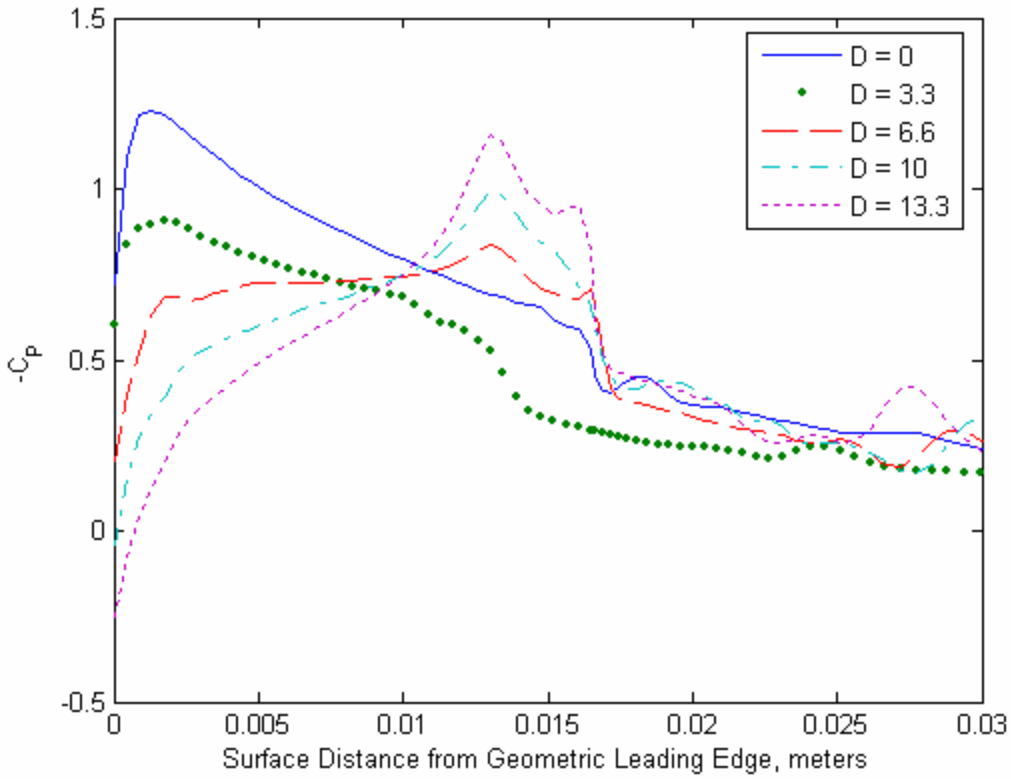

Figure 22. Pressure Distribution ($-C_P$) Over Model with and Ellipticity Ratio of Four and Various Droop Angles at Six Degrees Angle of Attack

The impacts of varying droop angle can be seen in Figure 22 where a blade model with an ellipticity ratio of 4 is run at six degrees angle of attack. For the case where there is no droop, a purely elliptical leading edge, the pressure spike occurs early, and has a comparatively high value. As the droop angle approaches the point where it closely matches the incidence angle, the magnitude of the pressure spike is the lowest. Further increases in the droop angle past the angle of attack result in the value of the pressure spike rising. Also, as the droop angle is increased, the point along the blade where the pressure spikes occur moves back away from the leading edge. The backside of the pressure spike shows the most dramatic decrease in the case where the droop angle is farthest past the angle of attack, suggesting an increase in the magnitude of the adverse pressure gradient and the formation of separation bubbles.

2. Boundary Layer Momentum Thickness

This section includes results for a selection of simulations that were run. The figures presented provide a generalization of the behavior of the boundary layer. The boundary layer momentum thickness was measured at a point 0.0350 meters along the body of the blade, approximately forty percent of the chord length. At this point, the local Reynolds number was 517,619. The boundary layer momentum thickness was arrived at by taking velocity data in the boundary layer at this point, and was reduced according to the equation

$$\theta = \int_0^\infty \frac{u}{U_\infty}\left(1 - \frac{u}{U_\infty}\right) dy \qquad (5)$$

The values graphically depicted in this section, and those tabulated in Appendix B represent the sum of the boundary layer momentum thickness on the pressure side (ps), and suction side (ss) of the model, $\theta_{ss} + \theta_{ps}$. Figure 21 shows an example of the boundary layers on the suction side and pressure side of the blade.

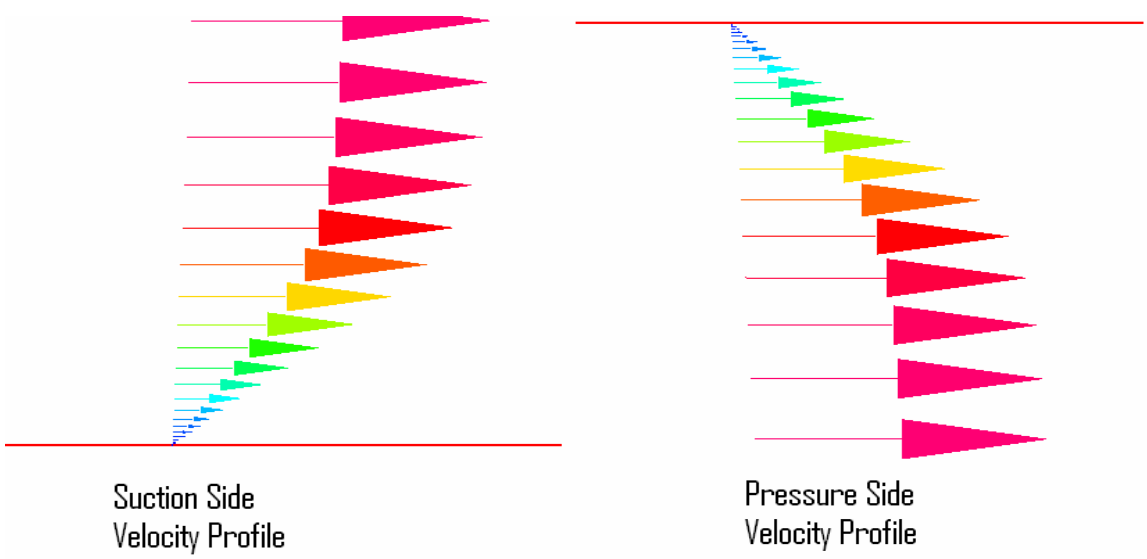

Figure 23. Velocity Profiles on the Suction Side (ss) and Pressure Side (ps) of a Plate as Used in the Calculation of the Boundary Layer Momentum Thickness, $\theta_{ss} + \theta_{ps}$

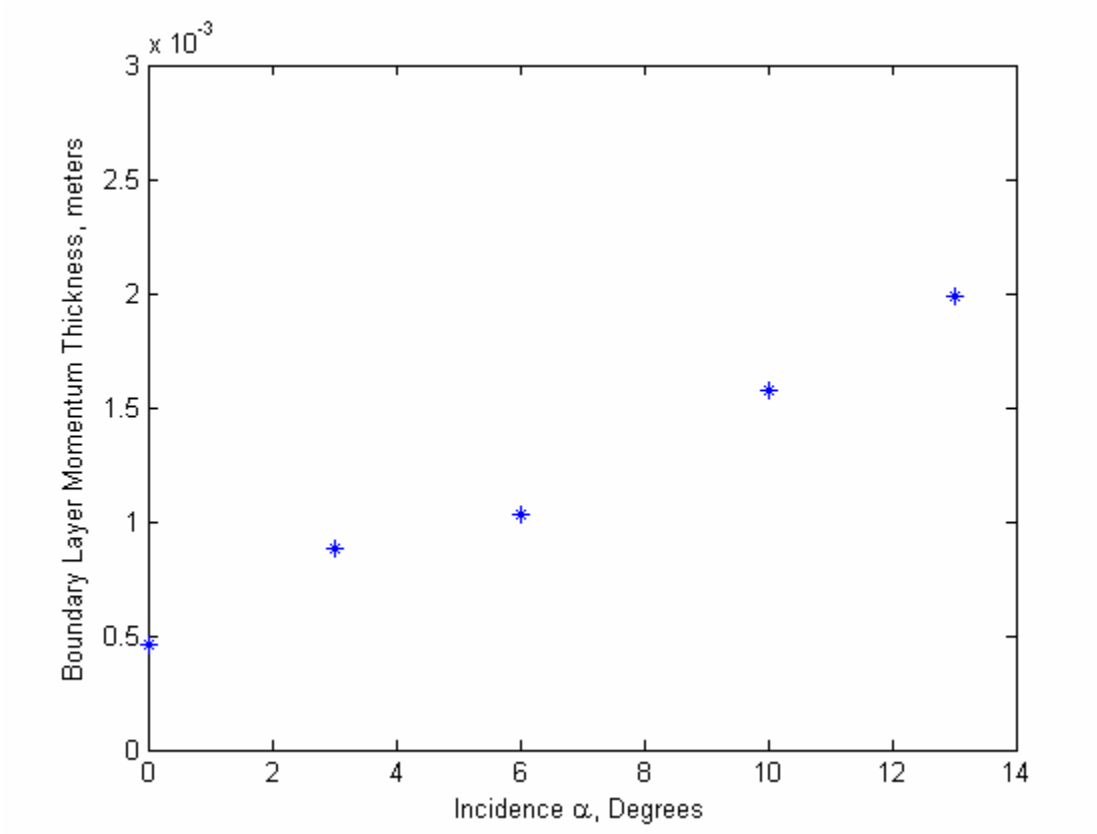

Figure 24. Circular Leading-Edge Boundary Layer Momentum Thickness, $\theta_{ss} + \theta_{ps}$, at Various Angles of Attack

Returning to the baseline geometry of a circular leading-edge shape, Figure 24 depicts the impact of angle of attack on the boundary layer momentum thickness. In the case of the circular leading edge, these values were obtained based on calculated velocity profiles taken at the trailing edge of the model. The separation that occurred on the circular leading-edge model made calculating the boundary layer momentum thickness at the original calculation point unviable. However, for the undrooped, zero incidence simulations, measurements made father down the blade where the flow had reattached allowed for this calculation. From Figure 24, it can be seen that the boundary layer momentum thickness increases as angle of attack increases. Clearly the thickness is not linearly dependent on angle of attack, and the increase becomes more dramatic at higher incidences.

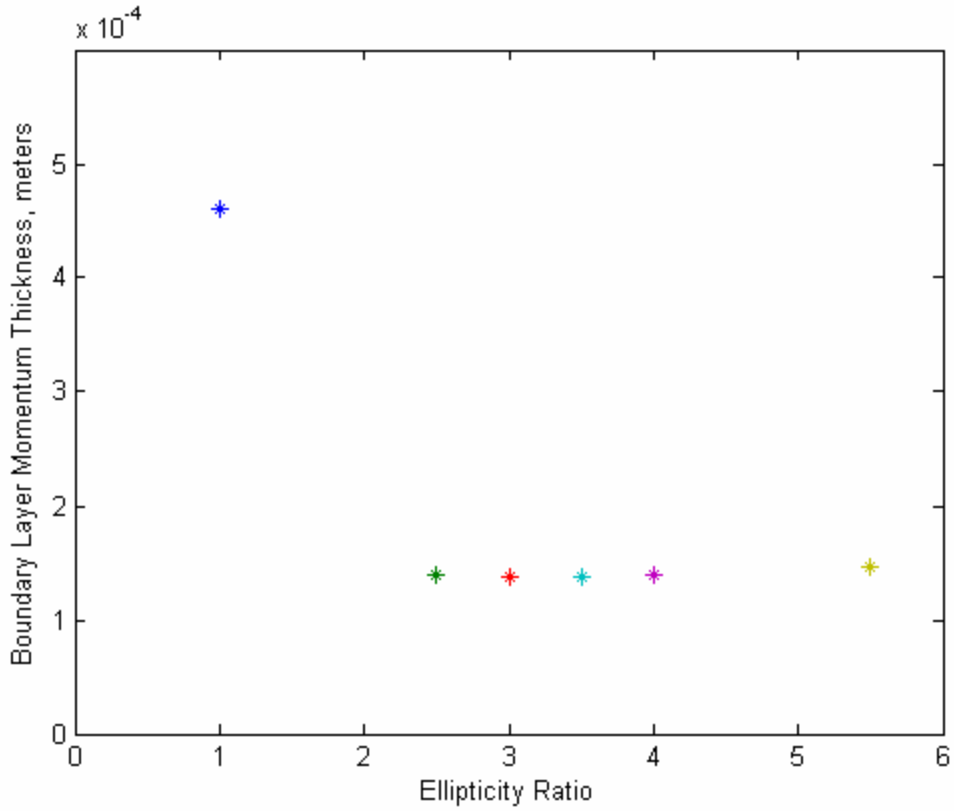

Figure 25. Momentum Thickness, $\theta_{ss} + \theta_{ps}$, at the End of the Plate for Various Ellipticity Models

Determining the effect of leading-edge ellipticity on aerodynamic losses was done by comparing the boundary layer momentum thicknesses as depicted in Figure 25. As the figure shows, the momentum thickness of the circular leading edge is several times that of the elliptic leading-edge models. With no droop, the blade model that experienced the least losses had an ellipticity ratio of three. A very shallow loss bucket can be seen in the momentum thicknesses of the blades with neighboring ellipticity ratios.

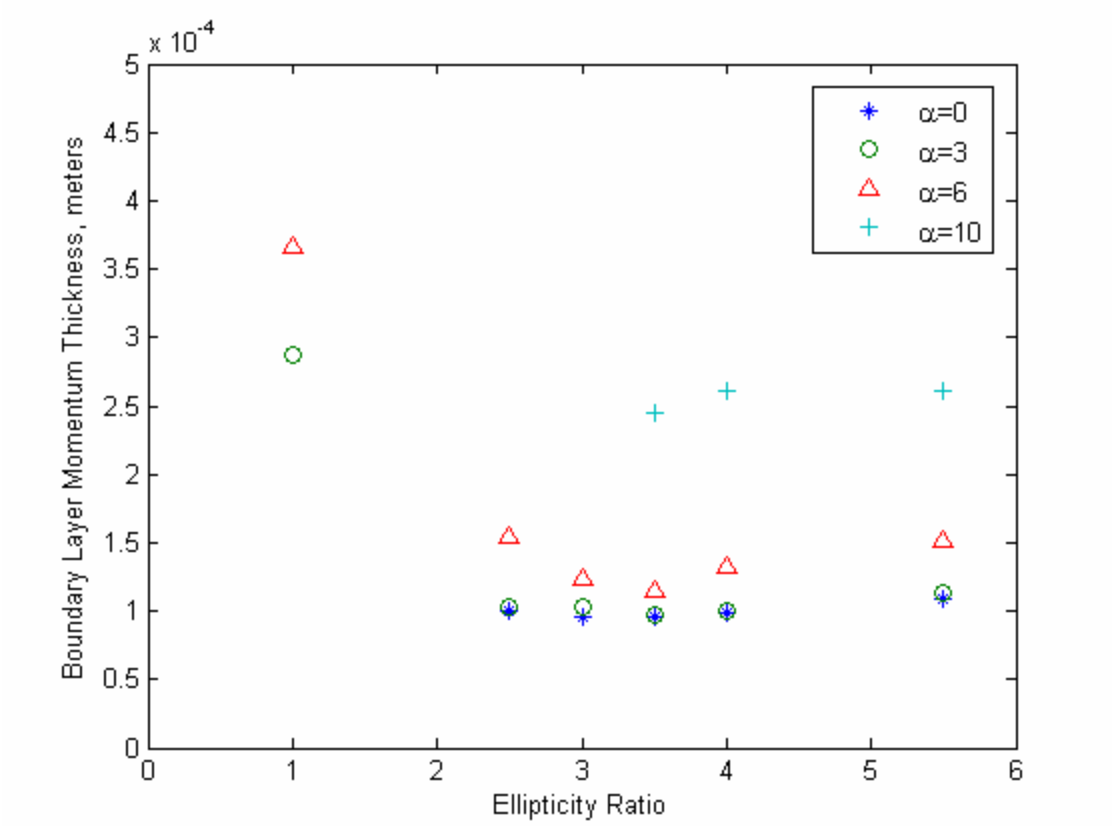

Figure 26. Boundary Layer Momentum Thickness, $\theta_{ss} + \theta_{ps}$, for All Ellipticities at Various Angles of Attack and Zero Degrees Droop

Again, as is seen in Figure 26, the circular leading-edge model experienced significantly higher losses that did the elliptic leading-edge models. This figure compares the effect of angle of attack on the boundary layer momentum thickness, and demonstrates that the thickness increases with increasing angle of attack. Figure 26 does not have any thickness values at an incidence of 13 degrees because all models experienced separation at the point of boundary layer momentum thickness calculations at this incidence. Additionally, only the models with an ellipticity ratio of 3.5 and higher had attached flow at an incidence of ten degrees. The blade model with an ellipticity ratio of 3.5 showed the least dependency on angle of attack, having the tightest grouping of momentum thicknesses, and only separating at 13 degrees incidence. The blade model with an ellipticity ratio of 5.5 experienced slightly higher losses that those of the less elliptic blades. This can partially be attributed to the increased surface distance the flow has to travel, which results in a slightly higher boundary layer momentum thickness.

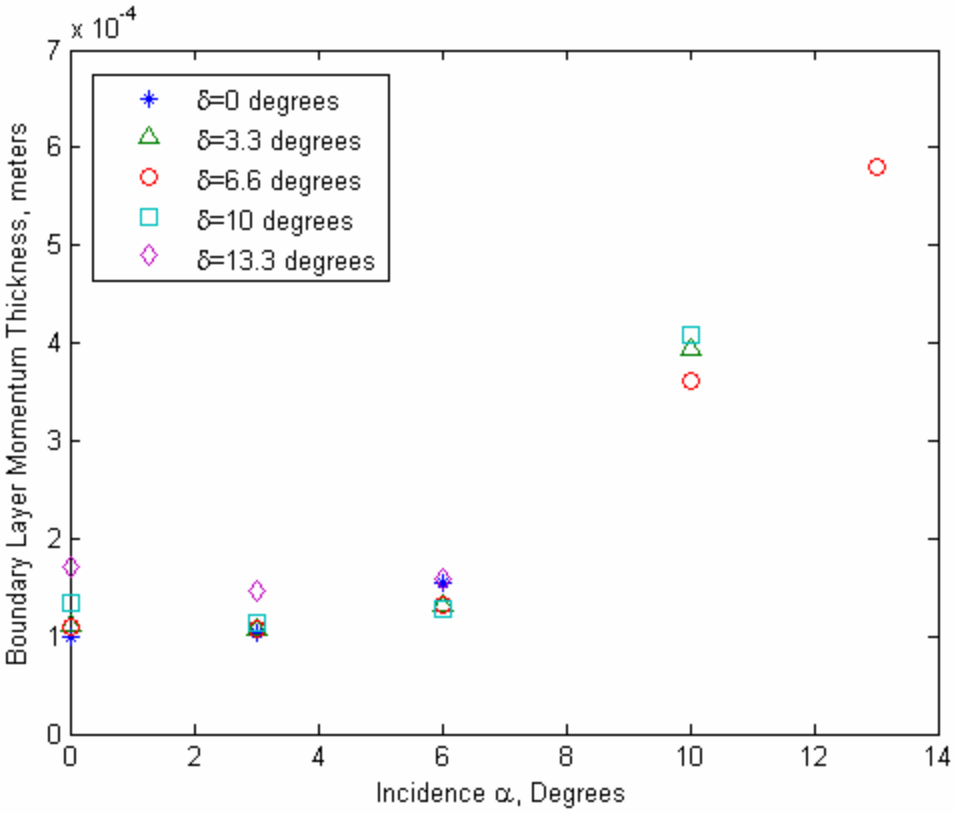

Figure 27. Boundary Layer Momentum Thickness, $\theta_{ss} + \theta_{ps}$, for Model with Leading-Edge Ellipticity Ratio of 2.5 and All Droop Angles at Various Angles of Attack

Analyzing the effects of droop on the blade model with an ellipticity ratio of 2.5, Figure 27 shows that the boundary layer momentum thickness increases with incidence. Separation was again experienced at an angle of attack of 13 degrees for all droops except the six degree case. At the lower incidences, six degrees for example, the lowest losses are observed for the models where the droop angle is just slightly higher than the incidence angle. In this case, drooping the leading edge to six degrees, or even 10 degrees, achieved lower losses than no droop or drooping it to 13 degrees.

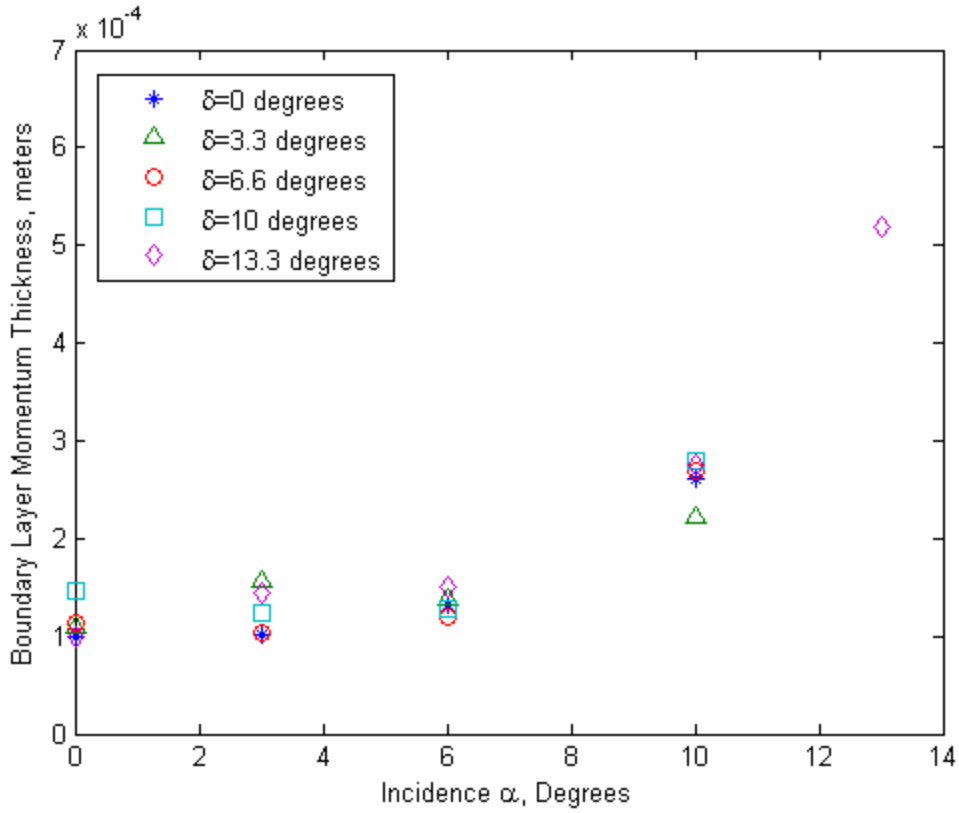

Figure 28. Boundary Layer Momentum Thickness, $\theta_{ss} + \theta_{ps}$, for Model with Ellipticity Ratio of Four and All Droop Angles at Various Angles of Attack

A similar trend to that depicted in Figure 27 is seen in Figure 28. In general, the boundary layer momentum thickness increases with increasing angle of attack. However, drooping to where the δ angle more closely match the incidence angle, α results in lower losses than an undrooped leading edge at incidence.

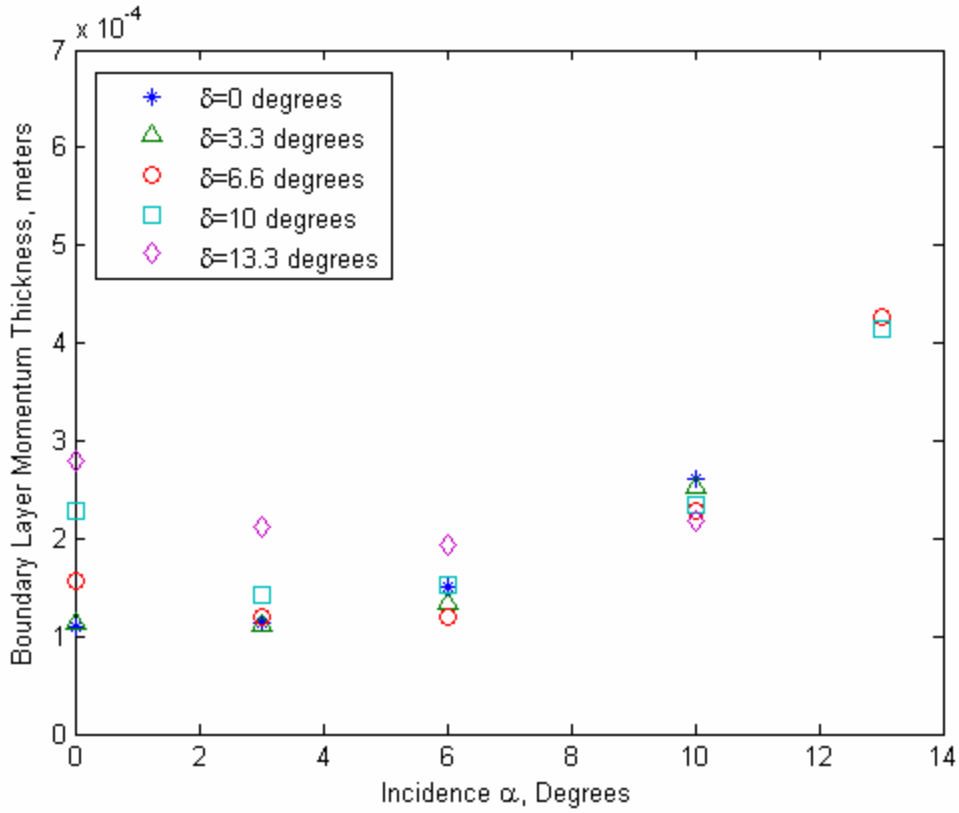

Figure 29. Boundary Layer Momentum Thickness, $\theta_{ss} + \theta_{ps}$, for Model With Ellipticity Ratio of 5.5 and All Droop Angles at Various Angles of Attack

At the highest ellipticity ratio tested, 5.5, it can be seen that drooping the leading edge still is mostly beneficial when compared to the undrooped case. However, as Figure 29 exemplifies, at very low incidences, drooping the leading edge can result in higher losses that it would at higher angles of attack. In this case, it can be seen that the greatest reduction in losses occurs for the models that have a droop angle closely matching the incidence, indicating the impact of aligning the leading-edge direction with the angle of attack to reduce losses.

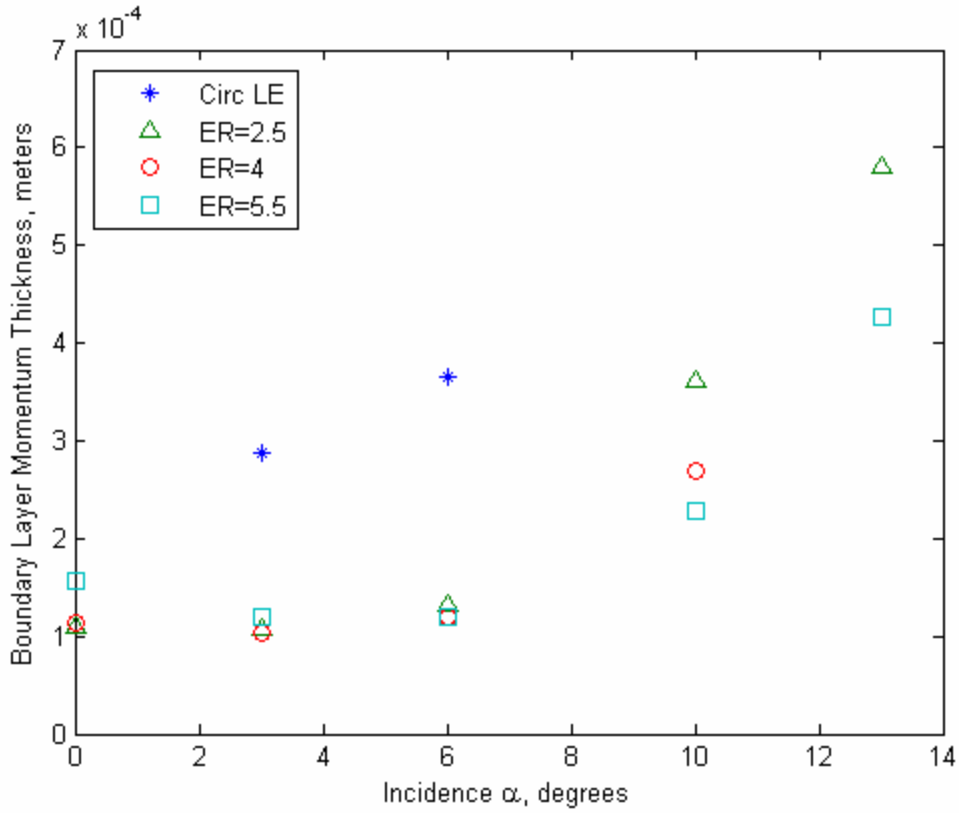

Figure 30. Boundary Layer Momentum Thickness, $\theta_{ss} + \theta_{ps}$, for Models of All Ellipticity Ratios with 6.6 Degrees Droop at Various Angles of Attack

In Figure 30, the effects of ellipticity with constant droop are examined at various angles of attack. In the cases where the flow was attached at the point of boundary layer momentum calculation, the circular leading edge has losses several times those of the elliptic leading edges. Also, from Figure 30, it can be seen that the lowest losses occur near the point where the incidence most closely matches the droop angle.

B. DISCUSSION OF FLOW FIELDS

The results provided give insight into the impact of the leading-edge geometry on the pressure distribution and boundary layer momentum thickness. Analyzing these results allows for the indication of boundary layer control as well as the losses that are present at a result of the geometry modification.

Calculations made on the baseline geometry of a flat plate with a circular leading edge, allowed for the determination of whether or not a particular ellipticity and droop angle were advantageous at a certain angle of attack. The circular leading-edge model

experienced heavy separation at the leading edge, which resulted in poorly developed flow over the remaining surface of the blade on both the suction and pressure sides.

Even where the flow reattached, a separation bubble formed. Figures 31 and 32 show a close up of these separation bubbles on the suction side and pressure side, respectively, where the velocity vectors are represented by arrows. As the figures show, in the separation bubble the large adverse pressure gradient results in the flow actually traveling backwards.

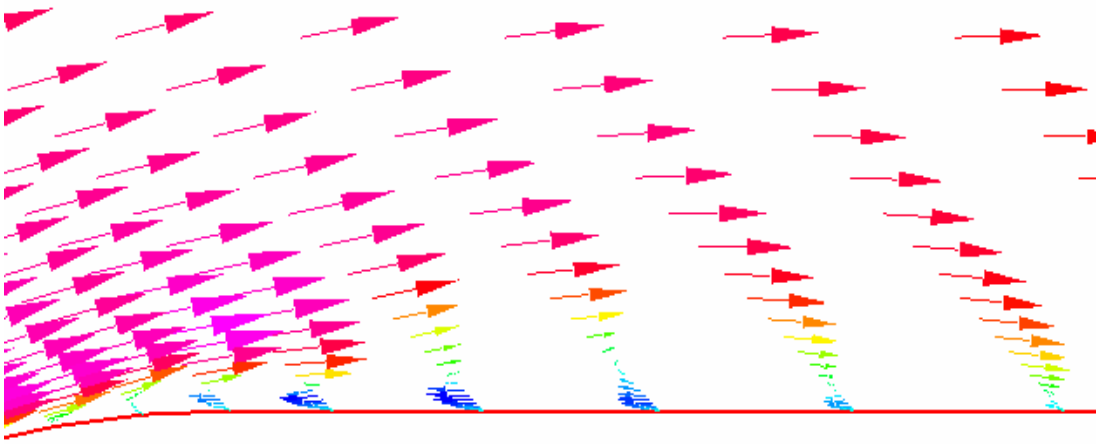

Figure 31. Leading-Edge Suction Side Separation Bubble

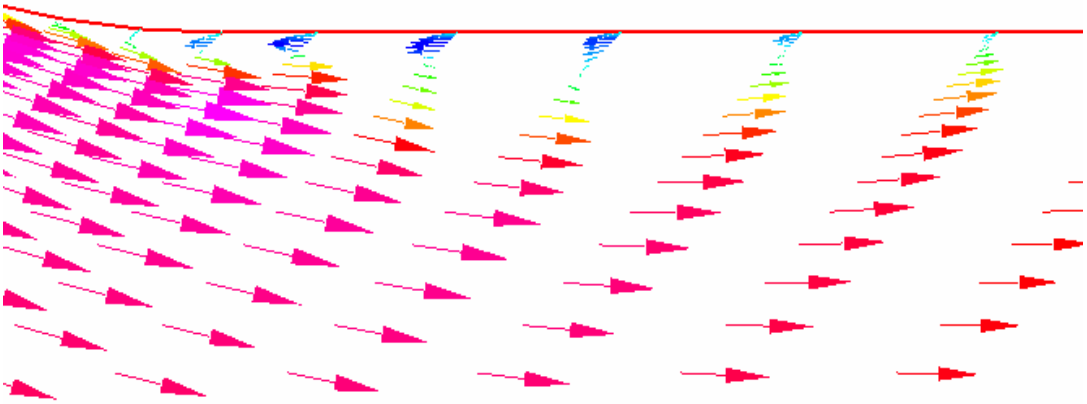

Figure 32. Leading-Edge Pressure Side Separation Bubble

A blade with a higher ellipticity ratio allowed for better control of the flow over the leading edge, as seen in Figure 33. Looking at the flow over the suction side of the leading edge shows that even at an angle of attack of ten degrees, the flow is better controlled than in the case of the circular leading edge. However, at the higher angles of attack, such as shown in Figure 33, the flow still separates and transitions to turbulence, however the region of separated flow is not as dramatic as for the circular leading-edge model. In fact, the only models for which no separation was noticeable over the entire blade body had ellipticity ratios of four and 5.5 with zero degrees droop, run at zero degrees incidence.

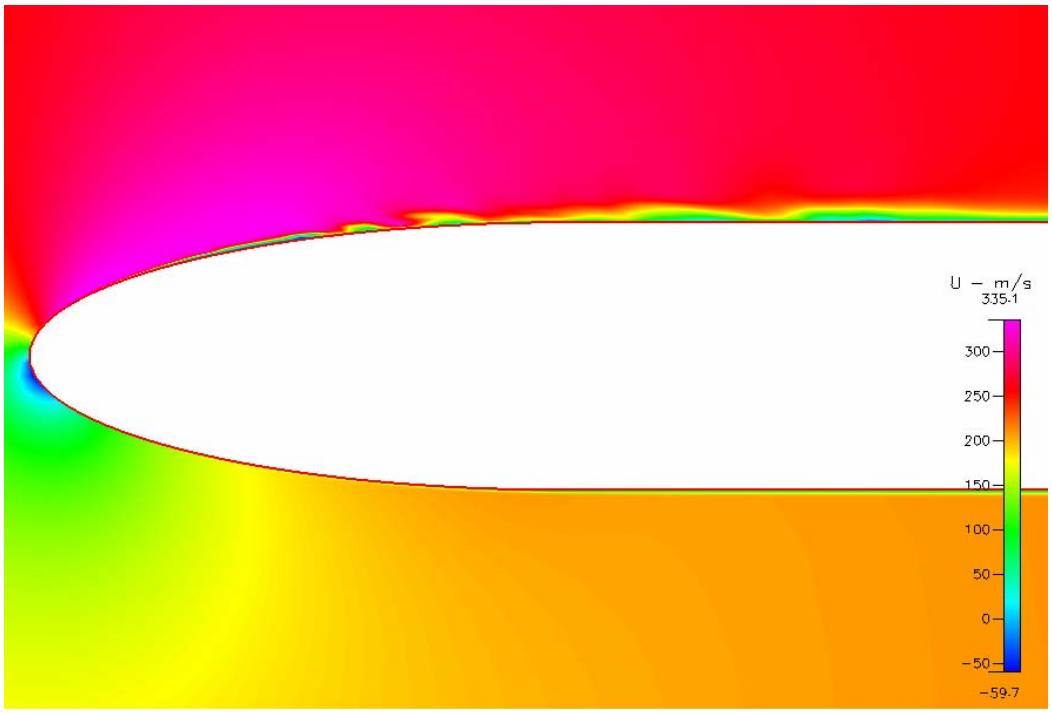

Figure 33. Leading-Edge View of Blade Model with Ellipticity Ratio of 4, Zero Degrees Droop, Ten Degrees Incidence

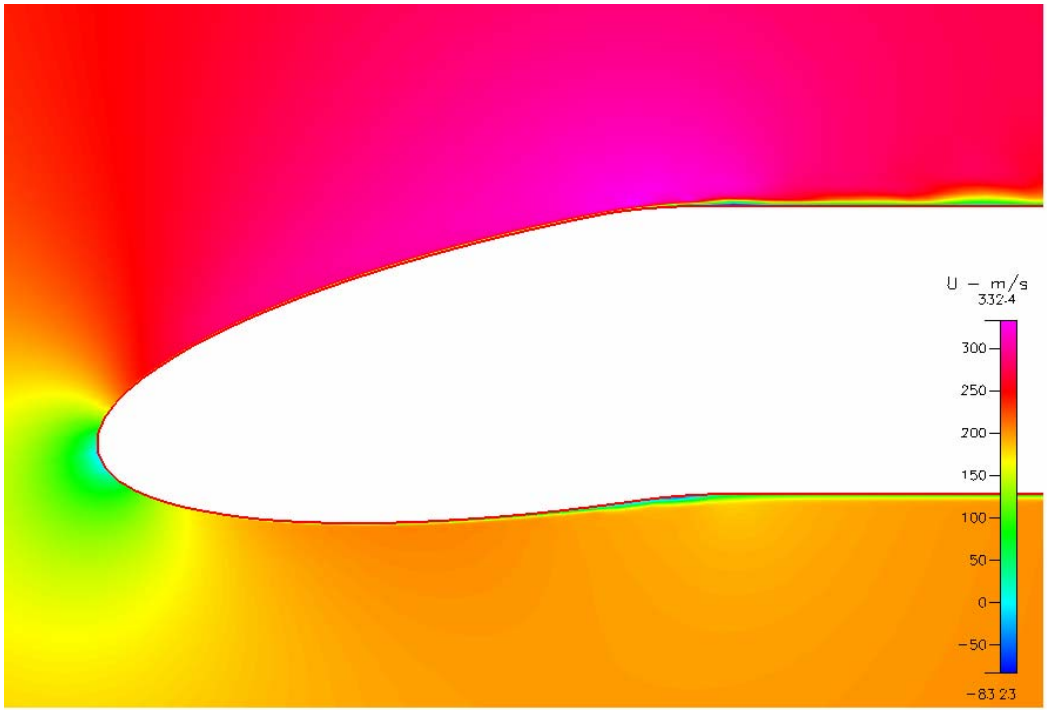

Figure 34. Leading-Edge View of Blade Model with Ellipticity Ratio of 4, Ten Degrees Droop, Zero Degrees Incidence

Despite the apparent advantages of the drooped, elliptic leading edge, there was a more distinct impact on the flow over the pressure side of the airfoil at lower angles of attack. Figure 34 shows that when the droop angle is far greater than the incidence, the velocity boundary layer grows much quicker on the pressure side than it did for the undrooped case. This actually results in a separation bubble forming at the point where the leading edge and the blade body are blended on the pressure side. This separation bubble decreases in size and eventually vanishes as the droop angle is brought closer to the angle if incidence. On the suction side, the separation bubbles also decreased in size as incidence more closely match the droop angle.

The results presented for the boundary layer momentum thickness are more valuable qualitatively than quantitatively. The prediction of transition from laminar to turbulent flow still remains difficult, and the tools necessary to predict this transition as applied to the cases run are not available. The exact values arrived at for boundary layer momentum thickness hold less importance than the trend of these values. The main benefit from this analysis is to see the effects of leading-edge geometry modification. A relative comparison of the momentum thickness between the different cases simulated

allows for the impact of leading-edge ellipticity and droop to be observed. Appendix A provides a listing of all cases simulated, and whether or not separation occurred on the suction side and pressure side near the leading edge. Also, it is indicated whether or not there was separation at the point of velocity measurements used for the calculation of boundary layer momentum thickness. Appendix B provides boundary layer momentum thickness values for all cases. These calculations were made at a consistent point along the plate, however for comparison purposes, it was necessary in certain instances to provide this calculation at the end of the model, or the trailing edge, as indicated by a (TE).

IV. CONCLUSIONS AND RECOMMENDATIONS

Based on the numerical simulations performed, the following conclusions were drawn:

1. The performance and ability of ESI-CFD to provide results acceptably close to experimental values was verified. The pressure distribution over the Walraevens Cumpsty model provided a trend that was as close as expected to the experimental results.

2. Numerical results for all simulations were obtained. Pressure distributions were calculated over the surface of each model that indicated boundary layer behavior. The boundary layer momentum thickness was calculated at a specified point on each model. In certain cases the point where the boundary layer momentum thickness was calculated had to be changed due to separation occurring at the initial calculation point.

3. Increasing the incidence that the models were simulated at generally resulted in a greater pressure spike, a greater adverse pressure gradient, and an increase in the likelihood of separation and transition to turbulence. Increasing the ellipticity allowed for smoother acceleration and deceleration of the flow over the leading edge. The greater the ellipticity, the less likely a separation bubble would occur. Drooping the leading edge to match the angle of attack resulted in the greatest reduction of losses. These reductions were not as substantial when the droop angle was less than or greater than the incidence angle.

4. An optimum ellipticity ratio lies somewhere in the 2.5 to 5.5 range. The model with an ellipticity ratio of 3 achieved the lowest losses at zero degrees incidence; however surrounding ellipticities achieved boundary layer momentum thicknesses that were very close. Over a range of incidences, the model with an ellipticity ratio of 3.5 displayed the lowest losses. An optimum droop angle does not exist over a range of

angle of attack. Rather, an optimum droop angle exists where the leading edge is drooped to most closely match the expected incidence. A moderate droop of 6.66 degrees did, however, show a reduction in losses over the incidence range when compared to a circular leading edge.

APPENDIX A. FLOW SEPARATION

Table 5 lists all the regimes tested, and are marked as to whether or not the flow separated on the blade. An X in the third column denotes whether or not there was leading-edge suction side separation. The fourth column denotes whether or not the flow separated on the pressure side of the leading edge. An X in the sixth column indicates that the flow was separated where velocity measurements were made on the suction side of the blade to measure the boundary layer momentum thickness. This indicates that measurements taken at this point were not used in the calculation of the momentum boundary layer thickness. For undrooped, zero incidence cases where this occurred, the momentum thickness was recalculated at the trailing edge for comparison reasons.

Table 5. Simulation Matrix Indicating Separated Flows Schemes

Ellipticity Ratio	Droop Angle	Incidence	Suction Side Leading-Edge Separation	Pressure Side Leading-Edge Separation	Separated Flow at Point of θ Measurement
0.625	0	0	X	X	X
0.625		3	X	X	X
0.625		6	X	X	X
0.625		10	X	X	X
0.625		13	X		
1	0	0	X	X	X
1		3	X	X	
1		6	X	X	
1		10	X	X	X
1		13	X		
2.5	0	0	X		
		3	X		
		6	X		
		10	X		X
		13	X		X
2.5	3.333	0	X	X	
		3	X	X	
		6	X	X	
		10	X	X	
		13	X		X

2.5	6.666	0	X	X	
		3	X	X	
		6	X		
		10	X		
		13	X		
2.5	10	0	X	X	
		3	X	X	
		6	X	X	
		10	X	X	
		13	X		X
2.5	13.333	0	X	X	
		3	X	X	
		6	X	X	
		10	X	X	X
		13	X		X
3	0	0	X	X	
		3	X		
		6	X		
		10	X		X
		13	X		X
3.5	0	0			
		3	X		
		6	X		
		10	X		
		13	X		X
4	0	0			
		3	X		
		6	X		
		10	X		
		13	X		X
4	3.333	0		X	
		3			
		6	X		
		10	X		
		13	X		X
4	6.666	0		X	
		3		X	
		6	X	X	
		10	X		

		13	X		X
4	10	0	X	X	
		3	X	X	
		6	X	X	
		10	X	X	
		13	X	X	X
4	13.333	0	X	X	
		3	X	X	
		6	X	X	
		10	X	X	
		13	X	X	
5.5	0	0			
		3	X		
		6	X		
		10	X		
		13	X		X
5.5	3.333	0		X	
		3	X	X	
		6	X		
		10	X		
		13	X		X
5.5	6.666	0	X	X	
		3	X	X	
		6	X	X	
		10	X	X	
		13	X		
5.5	10	0	X	X	
		3	X	X	
		6	X	X	
		10	X	X	
		13	X	X	
5.5	13.333	0	X	X	
		3	X	X	
		6	X	X	
		10	X	X	
		13	X	X	X

THIS PAGE INTENTIONALLY LEFT BLANK

APPENDIX B. TABULATED CALCULATIONS

Table 6. Boundary Layer Momentum Thicknesses

Ellipticity Ratio		Droop Angle (deg)	Incidence (deg)	Momentum Thickness (meters)
0.625		0	0	0.00013992659014 (TE)
0.625			3	-------
0.625			6	-------
0.625			10	-------
0.625			13	0.00212813723579
1		0	0	-------
1			3	0.00028797913689
1			6	0.00036587474820
1			10	-------
1			13	-------
1		0	0	0.000460385996270825 (TE)
1			3	0.00087850425430968 (TE)
1			6	0.00103134429584577 (TE)
1			10	0.00157126980558499 (TE)
1			13	0.00198567433925469 (TE)
2.5		0	0	0.000100094059520359
			3	0.000103623994917905
			6	0.000154502573900588
			10	-------
			13	-------
2.5		0	0	0.000140104356256184 (TE)
			3	0.000296696428376302 (TE)
			6	0.000539087536161559 (TE)
			10	0.00111492335987182 (TE)
			13	0.0017212911378331 (TE)
2.5		3.333	0	0.000111940154827703
			3	0.000107007881792047
			6	0.000132018572754849
			10	0.000393112974704518
			13	-------
2.5		6.666	0	0.00010999359999889
			3	0.000106563326027226
			6	0.000131588168817812
			10	0.000361654408114119

			13	0.000580175862682864
2.5		10	0	0.000135036565426467
			3	0.000112853954569468
			6	0.000128443059324597
			10	0.000408886437067048
			13	-------
2.5		13.333	0	0.000170979688948428
			3	0.000146508049516922
			6	0.000157988001399255
			10	-------
			13	-------
3		0	0	9.62451589779253e-005
			3	0.000103487255926937
			6	0.000123698773002648
			10	-------
			13	-------
3		0	0	0.000137071890747477 (TE)
			3	0.000143351992026842 (TE)
			6	0.000312874597826619 (TE)
			10	0.000609292125163118 (TE)
			13	0.00114217567150724 (TE)
3.5		0	0	9.64665416381034e-005
			3	9.66500958278449e-005
			6	0.000114786381077528
			10	0.000245160912298984
			13	-------
3.5		0	0	0.000137133877584776 (TE)
			3	0.000284432864031436 (TE)
			6	0.000253960077912356 (TE)
			10	0.000996840707000437 (TE)
			13	0.00151375449643012 (TE)
4		0	0	9.91151996796203e-005
			3	0.000100799819994302
			6	0.000132939671289602
			10	0.000261315087653351
			13	-------
4		0	0	0.000138743363673526 (TE)
			3	0.000255392430163375 (TE)

			6	0.000445981647430393 (TE)
			10	0.000989769680758431 (TE)
			13	0.00146601906201849 (TE)
4		3.333	0	0.000108607995415983
			3	0.000156897360736471
			6	0.000137921291202453
			10	0.000222408961994281
			13	-------
4		6.666	0	0.000113998789841625
			3	0.000102489628318904
			6	0.000120473186067883
			10	0.000268641267614245
			13	-------
4		10	0	0.000146579054343001
			3	0.000123489211348902
			6	0.000127947480025751
			10	0.000279193604482142
			13	-------
4		13.333	0	0.000138743363673526
			3	0.000143990367228108
			6	0.000150338269765518
			10	0.000275856745376864
			13	0.000518584040505425
5.5		0	0	0.00010956377911036
			3	0.000113821131530337
			6	0.000151073339792549
			10	0.000260962439215612
			13	-------
5.5		0	0	0.00014639467646804 (TE)
			3	0.000229817286670545 (TE)
			6	0.000391688112817612 (TE)
			10	0.000864179667221954 (TE)
			13	0.00121485431117817 (TE)
5.5		3.333	0	0.00011403299906077
			3	0.000112559125041705
			6	0.000134908717749009
			10	0.000252724002722503
			13	-------
5.5		6.666	0	0.000156694446737734

			3	0.000118824232513354
			6	0.000120257303307709
			10	0.000227403778759464
			13	0.000426332114164971
5.5		10	0	0.000229040192077047
			3	0.000143260860137492
			6	0.000151942563489376
			10	0.000235032091887678
			13	0.000414957837651133
5.5		13.333	0	0.000280146166201907
			3	0.000212539361753376
			6	0.000193542663084542
			10	0.000218797975590369
			13	-------

APPENDIX C. PRESSURE DISTRIBUTION PLOTS

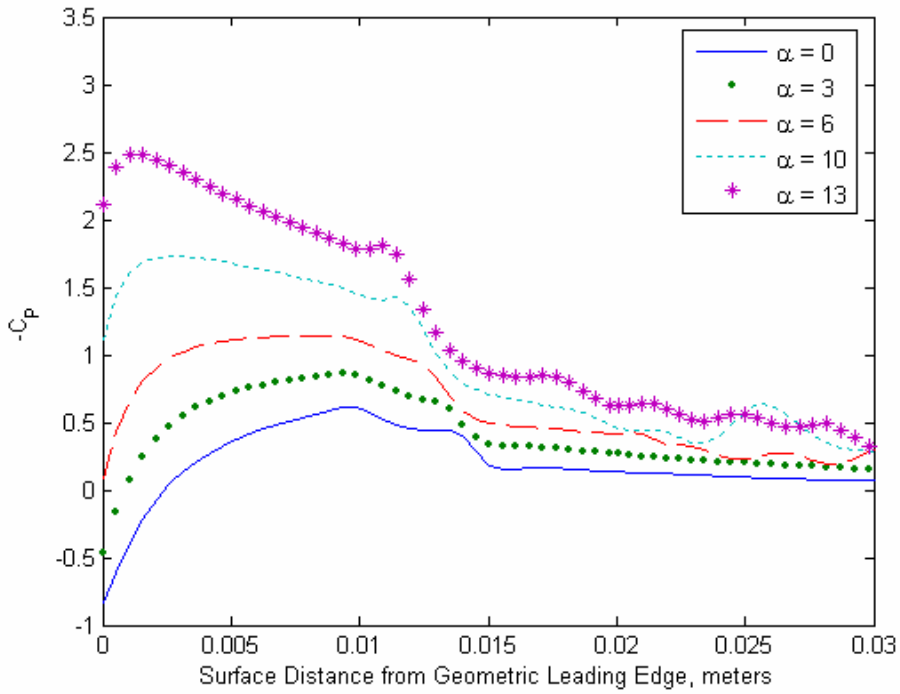

Figure 35. Pressure Coefficient ($-C_P$) over Model from Geometric Leading Edge with Ellipticity Ratio of 2.5 and Droop Angle of 3.33 degrees

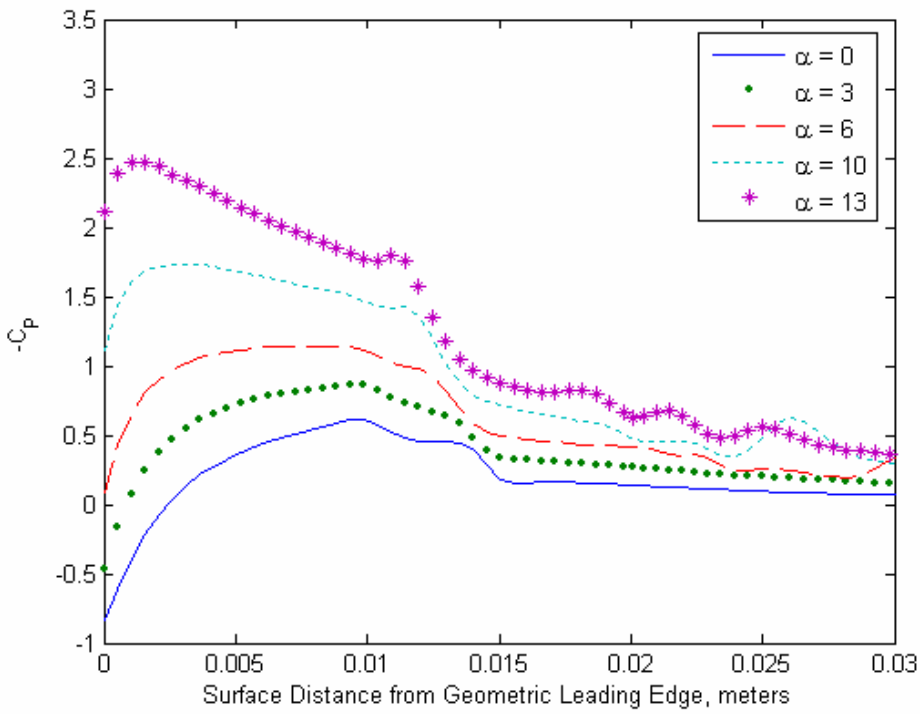

Figure 36. Pressure Coefficient ($-C_P$) over Model from Geometric Leading Edge with Ellipticity Ratio of 2.5 and Droop Angle of 6.66 degrees

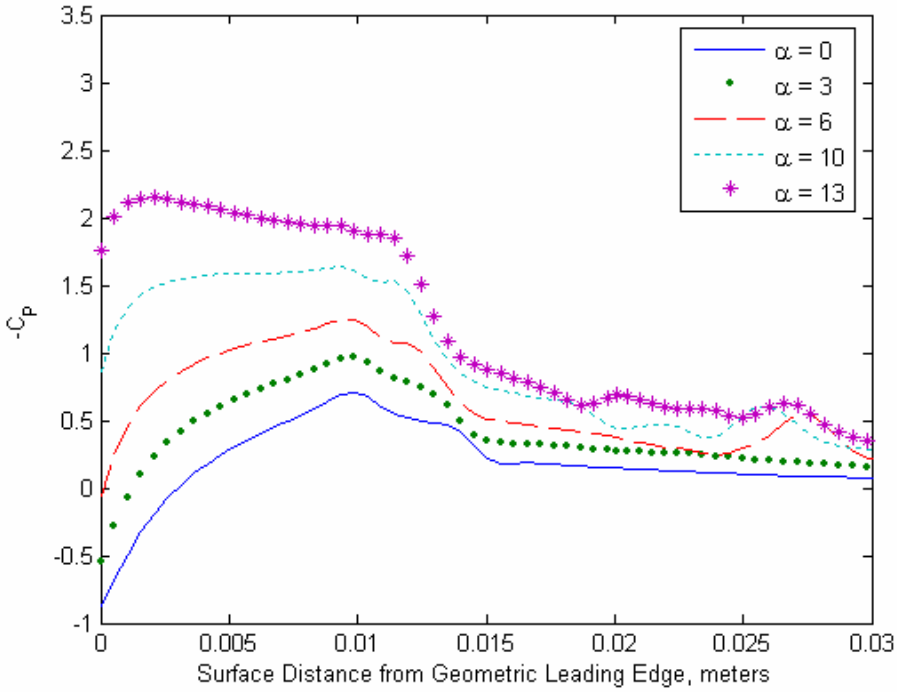

Figure 37. Pressure Coefficient ($-C_P$) over Model from Geometric Leading Edge with Ellipticity Ratio of 2.5 and Droop Angle of 10.0 degrees

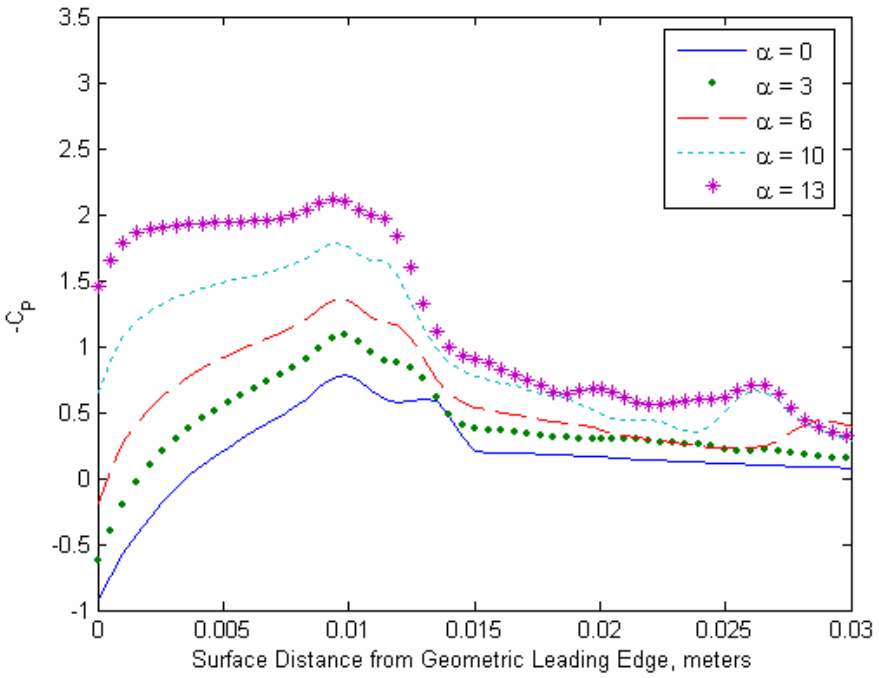

Figure 38. Pressure Coefficient ($-C_P$) over Model from Geometric Leading Edge with Ellipticity Ratio of 2.5 and Droop Angle of 13.33 degrees

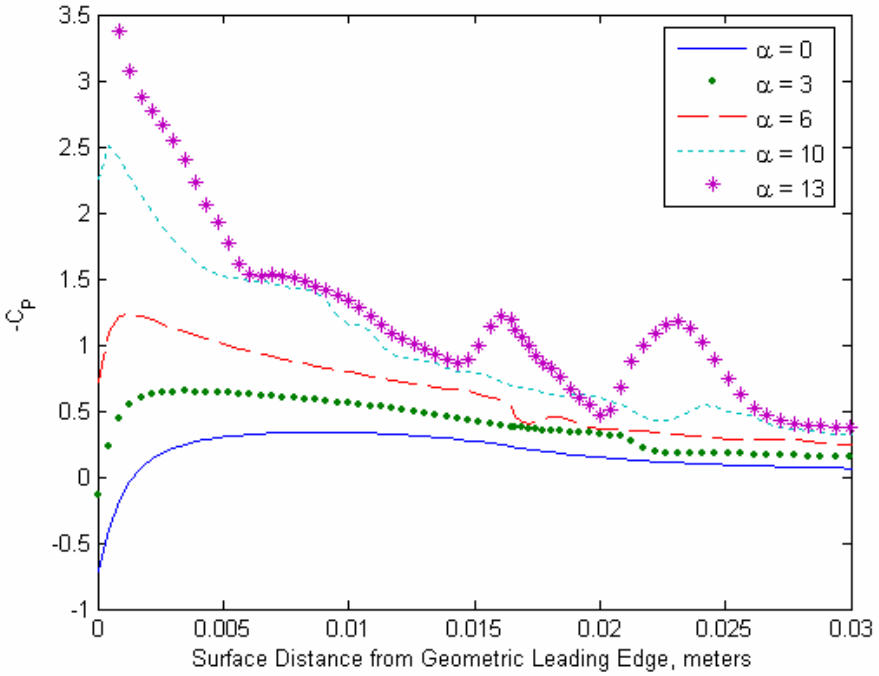

Figure 39. Pressure Coefficient ($-C_P$) over Model from Geometric Leading Edge with Ellipticity Ratio of 4.0 and Droop Angle of 0.0 degrees

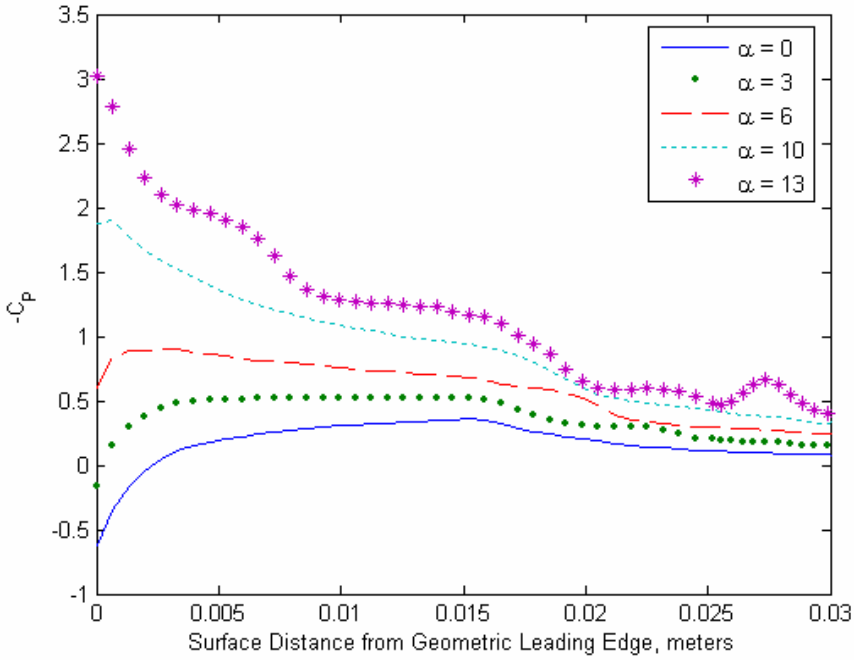

Figure 40. Pressure Coefficient ($-C_P$) over Model from Geometric Leading Edge with Ellipticity Ratio of 4.0 and Droop Angle of 3.33 degrees

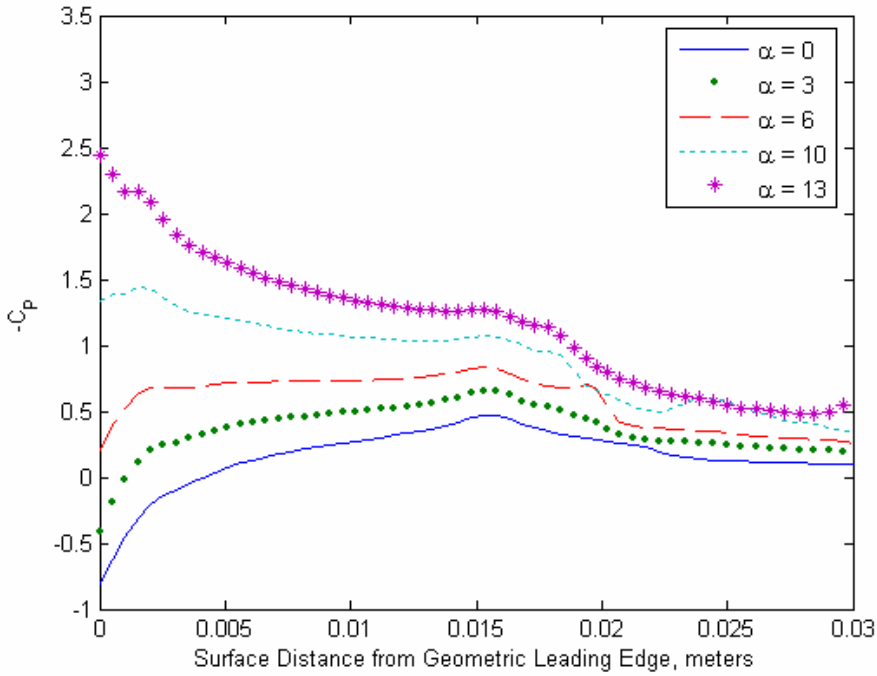

Figure 41. Pressure Coefficient ($-C_P$) over Model from Geometric Leading Edge with Ellipticity Ratio of 4.0 and Droop Angle of 6.66 degrees

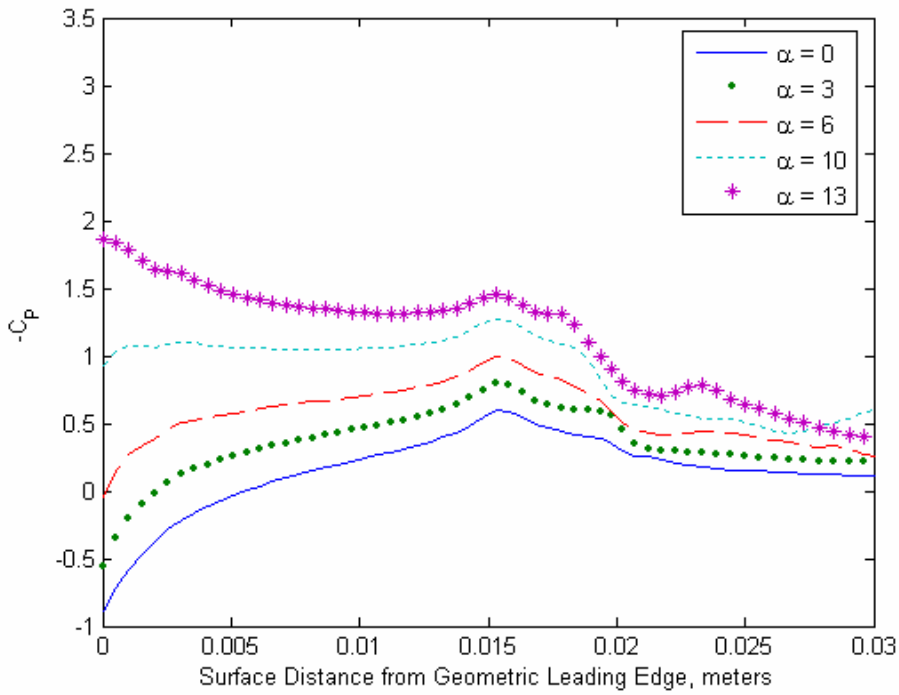

Figure 42. Pressure Coefficient ($-C_P$) over Model from Geometric Leading Edge with Ellipticity Ratio of 4.0 and Droop Angle of 10.0 degrees

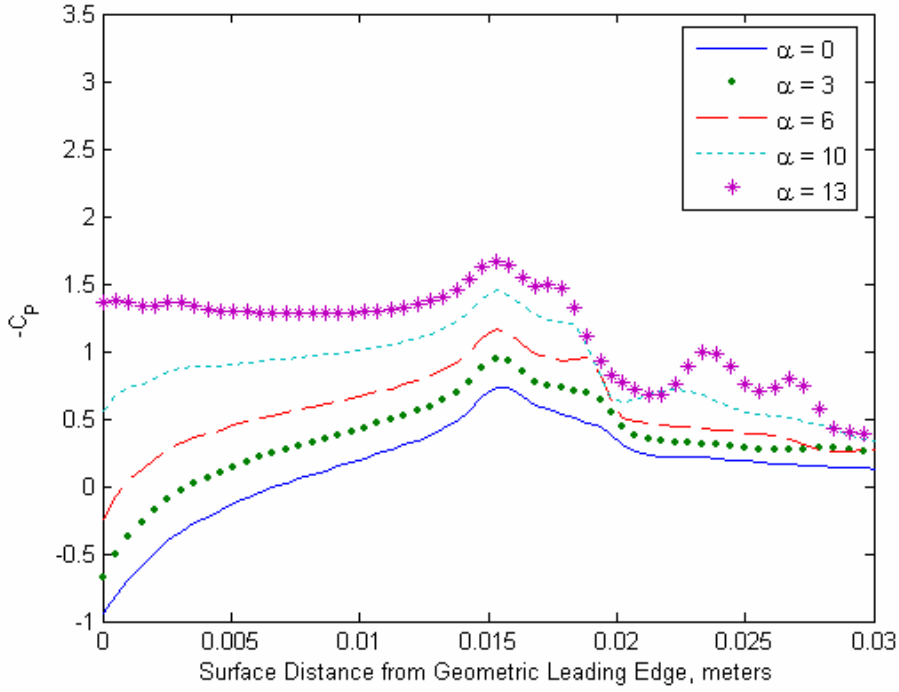

Figure 43. Pressure Coefficient ($-C_P$) over Model from Geometric Leading Edge with Ellipticity Ratio of 4.0 and Droop Angle of 13.33 degrees

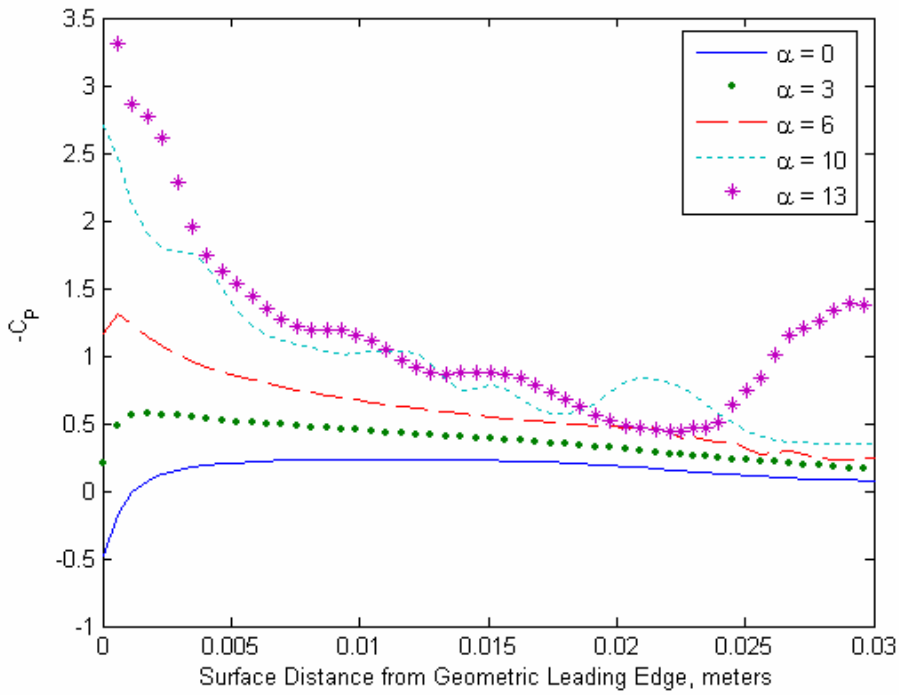

Figure 44. Pressure Coefficient ($-C_P$) over Model from Geometric Leading Edge with Ellipticity Ratio of 5.5 and Droop Angle of 0.0 degrees

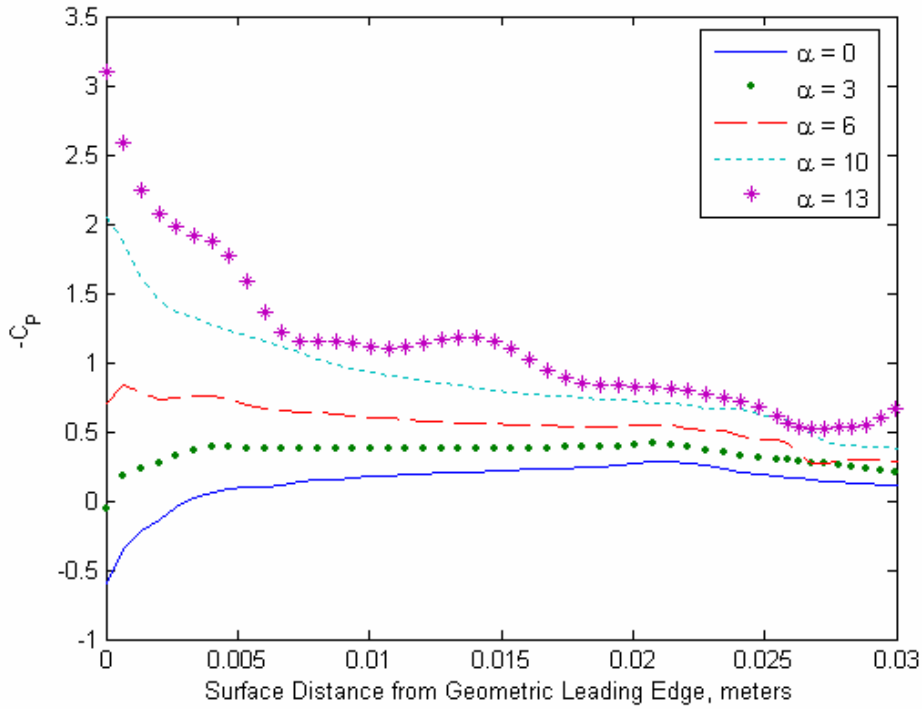

Figure 45. Pressure Coefficient ($-C_P$) over Model from Geometric Leading Edge with Ellipticity Ratio of 5.5 and Droop Angle of 3.33 degrees

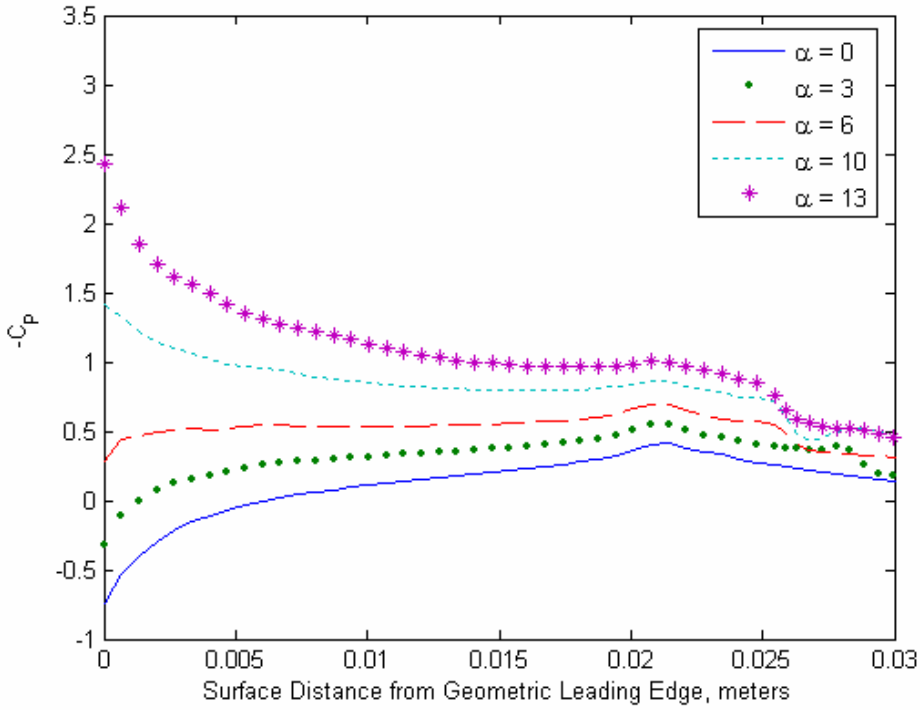

Figure 46. Pressure Coefficient ($-C_P$) over Model from Geometric Leading Edge with Ellipticity Ratio of 5.5 and Droop Angle of 6.66 degrees

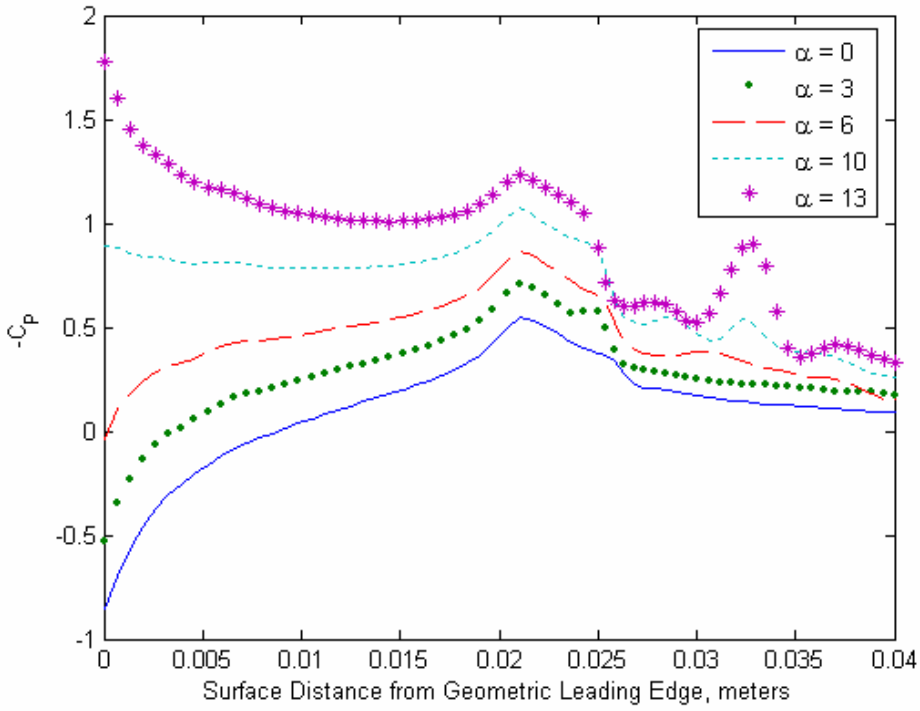

Figure 47. Pressure Coefficient ($-C_P$) over Model from Geometric Leading Edge with Ellipticity Ratio of 5.5 and Droop Angle of 10.0 degrees

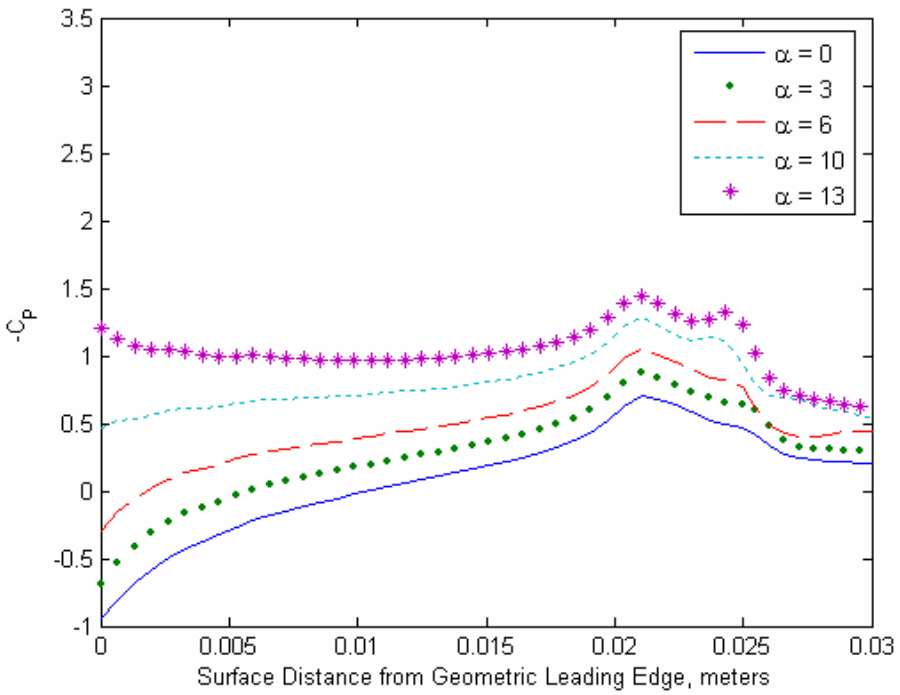

Figure 48. Pressure Coefficient ($-C_P$) over Model from Geometric Leading Edge with Ellipticity Ratio of 5.5 and Droop Angle of 13.3 degrees

APPENDIX D. MATLAB CODE

A. LEADING-EDGE BLENDING CODE

The following code was used to calculate the leading edge and plate geometries used in the simulations.

```
%%%%%%%%%%%%%%%%%%%%%%%%%%%%%%%%%%%%%%%%%%%%%%%%%%%%%%%%%%%%%%%%%%%
%Jonathan D. Powell
%Thesis Work
%This File Started 6 Mar 2005
%Flat Plate with a Modified Leading Edge
%Establish the flat plat
  % We'll make this flat plate approximately 8% thick (excluding leading
  % edge)
  clc
fp_x=0:0.5:100;
for i=1:length(fp_x)
fp_suct_y(i)=4;
fp_press_y(i)=-4;
end
%plot(fp_x,fp_suct_y,fp_x,fp_press_y)
%axis([-20 110 -30 30])
%axes equal
%*************
%Now to make modifications to the leading edge
%Starting with varying eccetricity of unrotated ellipse
b=fp_suct_y(1);
%incr=1:0.5:5.5;
incr=[1 2.5 4 5.5];
incr=incr(2)
a=b.*incr;
start=length(incr)/4;
stop=(3/4)*length(incr);
for i=1:length(incr)
  %for j=1:length(incr)
ecc(i)=sqrt(1-((b)^2)./((a(i)).^2));
[coord_x,coord_y] = ellipse1(0,0,[a(i) ecc(i)],0);
end
ecc=ecc';
```

```
%rot=0:15/(length(incr)-1):15;
rot=[0 3.33333 6.66667 10.0 13.33333];
rot=rot(5)
for j=1:length(incr)
  figure
   for k=1:length(rot)
   [coord_x_rot,coord_y_rot] = ellipse1(5,0,[a(j) ecc(j)],rot(k), [(75) (330)]);
%figure
%subplot(3,2,k)
   for tt=1:50
if ((coord_y_rot(tt)' < 4))
   y_tip_a(tt)=coord_y_rot(tt)';
else
   y_tip_a(tt)=fp_suct_y(1);
end
   end
      for pp=1:50
if  (min(coord_y_rot) < -4) & (coord_y_rot(100)' > -4)
   y_tip_b(pp)=coord_y_rot(pp+50)';
else
  y_tip_b(pp)=fp_press_y(1);
end
 y_tip=[y_tip_a y_tip_b];
   end
   for ss=1:15
      if y_tip_b(ss+35) > -4
         y_tip_b(ss+35)=fp_press_y(1);
      else
         y_tip_b(ss+35)=coord_y_rot(ss+85);
      end
   end
     y_tip=[y_tip_a y_tip_b];
   for xx=1:50
      if fp_x(xx) < coord_x_rot(1)
         fp_x_suct(xx)=coord_x_rot(1);
      else
         fp_x_suct(xx)=fp_x(xx);
      end
   end
        for rr=1:50
      if fp_x(rr)<coord_x_rot(100)
         fp_x_press(rr)=coord_x_rot(100);
      else
```

```
            fp_x_press(rr)=fp_x(rr);
          end
        end
          fp_x_suct_a=[fp_x_suct fp_x(50:200)];
        fp_x_press_a=[fp_x_press fp_x(50:200)];
            % plot(fp_x,fp_x_suct_y,fp_x,fp_x_press_y,coord_x_rot',coord_y_rot,'-')
%plot(fp_x_suct_a,fp_x_suct_y,fp_x_press_a,fp_x_press_y,coord_x_rot',y_tip,'.',coord_x_rot(1),y_tip(1),'*',coord_x_rot(100)',
y_tip(100),'*',coord_x_rot,coord_y_rot,5,0,'*',x,y,x_new,y_new,'.')
%axis equal
%axis([-10 20 -10 20])
%axis on
end
    end
x_lines=2:10;
a=coord_x_rot(3:5);
b=y_tip(3:5)';
p_a = polyfit(a,b,1);
m_a=p_a(1);
b=p_a(2);
c=coord_x_rot(14:16);
d=y_tip(14:16)';
p_c = polyfit(c,d,1);
m_c=p_c(1);
b_c=p_c(2);
y_c=-1/m_c*(x_lines-coord_x_rot(15))+y_tip(15);
for i=1:9
x_c_sta(i)=coord_x_rot(4);
end
pp_c=polyfit(x_lines,y_c,1);
y_cc=pp_c(1)*(coord_x_rot(4))+pp_c(2);
r_c=sqrt((coord_x_rot(15)-x_c_sta(1))^2+(y_tip(15)-y_cc)^2);
x_circ_c=coord_x_rot(15):0.3:coord_x_rot(4);
y_circ_c=sqrt(r_c^2-(x_circ_c-x_c_sta(1)).^2)+y_cc;
e=coord_x_rot(90:92);
f=y_tip(90:92)';
p_e=polyfit(e,f,1);
m_e=p_e(1);
b_e=p_e(2);
g=coord_x_rot(79:81);
g=coord_x_rot(79:81);
h=y_tip(79:81)';
p_g=polyfit(g,h,1);
m_g=p_g(1);
```

```
b_g=p_g(2);
y_g=-1/m_g*(x_lines-coord_x_rot(80))+y_tip(80);
for i=1:9
x_g_sta(i)=coord_x_rot(91);
end
pp_g=polyfit(x_lines,y_g,1);
y_gg=pp_g(1)*(coord_x_rot(91))+pp_g(2);
%r_g=sqrt((coord_x_rot(78)-x_g_sta(1))^2+(y_tip(78)-y_gg)^2);
r_g=sqrt((coord_x_rot(80)-x_g_sta(1))^2+(y_tip(80)-y_gg)^2);
x_circ_g=coord_x_rot(80):0.3:coord_x_rot(91);
y_circ_g=sqrt(r_g^2-(x_circ_g-x_g_sta(1)).^2)+y_gg;
x_circ_LE=0:0.1:5
y_circ_LE=sqrt(4^2-(x_circ_LE-5).^2)
coord_x_rot=[coord_x_rot(1:3)' fliplr(x_circ_c) coord_x_rot(16:77)' x_circ_g coord_x_rot(93:100)'];
y_tip=[y_tip(1:3) fliplr(y_circ_c) y_tip(16:77) y_circ_g y_tip(93:100)];
plot(fp_x_suct_a,fp_suct_y,fp_x_press_a,fp_press_y,coord_x_rot',y_tip,'.',coord_x_rot(1),y_tip(1),'*',coord_x_rot(length(c
oord_x_rot))',y_tip(length(y_tip)),'*',x_circ_g,y_circ_g,'*',x_circ_c,y_circ_c,'*',x_lines,y_g,x_g_sta,y_g)%,x_lines,y_c,x_c_sta,y_c,x_
g_sta(1),y_gg,'*')
%axis equal
%axis([-8 12 -10 10])
axis([-10 25 -25 10])
%end
%end
%runs_matrix_LE=[coord_x_rot' y_tip']
runs_matrix_fp_x=[fp_x_suct_a fp_x_press_a]';
runs_matrix_fp_y=[fp_suct_y fp_press_y]';
disp('X')
aaa=[coord_x_rot fp_x_suct_a fp_x_press_a]'
disp('Y')
aab=[y_tip fp_suct_y fp_press_y]'
%disp('FP X')
%aac=runs_matrix_fp_x
%disp('FP Y')
%aad=runs_matrix_fp_y
%runs_matrix_fp=[runs_matrix_fp_x runs_matrix_fp_y]
```

B. ELLIPTIC CALCULATIONS CODE

The MATLAB code below was used to calculate the ellipticity ratios of the undrooped models, and the arc length of their leading edges. These calculations were made based on the distance from the geometric leading edge, at the semimajor apex, to the point where the elliptic leading edge joined the plate body, at the semiminor apex.

```
ER=[0.625 1 2.5 3 3.5 4 5.5]
%Semiminor
a=[0.004];
%Semimajor
b=[0.625*a 1*a 2.5*a 3*a 3.5*a 4*a 5.5*a];
R_min=(b.^2)./a
R_maj=(a.^2)./b
t=0.008
s=(pi.*[3*(a+b)-sqrt((3*a+b).*(a+3*b))])/4
two_s_over_t=2*s./t

WalCump_circ_a=[0.0063];
WalCump_circ_b=[0.0063];
t_WalCump_circ=0.0126
WalCump_ellip_a=[0.0066];
WalCump_ellip_b=[0.0125];
t_WalCump_ellip=0.0132
s_WalCump_circ=(pi.*[3*(WalCump_circ_a+WalCump_circ_b)-
sqrt((3*WalCump_circ_a+WalCump_circ_b).*(WalCump_circ_a+3*WalCump_circ_b))])/4
s_WalCump_ellip=(pi.*[3*(WalCump_ellip_a+WalCump_ellip_b)-
sqrt((3*WalCump_ellip_a+WalCump_circ_b).*(WalCump_ellip_a+3*WalCump_ellip_b))])/4
two_s_over_t_WalCump_circ=2*s_WalCump_circ./t_WalCump_circ
%for elliptical model, in order to get a 2*s/t of 20, we need to go an
%additional 18.4292*t/2
extra_WalCump_circ=18.4292*t_WalCump_circ/2
%blendpoint for the circle is at 2s/t=1.5708
two_s_over_t_WalCump_ellip=2*s_WalCump_ellip./t_WalCump_ellip
%for elliptical model, in order to get a 2*s/t of 20, we need to go an
%additional 17.2816*t/2
extra_WalCump_ellip=17.2816*t_WalCump_ellip/2
%blendpoint for the ellips is at 2s/t=2.7184
plot(ER,s,'-*'), xlabel('Arclength on Ellipse from Semimajor Apex to Semiminor Apex, meters')
ylabel('Ellipticity Ratio')
vec=[0 0 0 0 0 0 0]
plotvec_x_1=[0,s(1)]
plotvec_x_2=[0,s(2)]
plotvec_x_3=[0,s(3)]
plotvec_x_4=[0,s(4)]
plotvec_x_5=[0,s(5)]
plotvec_x_6=[0,s(6)]
plotvec_x_7=[0,s(7)]
plotvec_y_1=[R_maj(1),R_min(1)]
plotvec_y_2=[R_maj(2),R_min(2)]
```

```
plotvec_y_3=[R_maj(3),R_min(3)]

plotvec_y_4=[R_maj(4),R_min(4)]

plotvec_y_5=[R_maj(5),R_min(5)]

plotvec_y_6=[R_maj(6),R_min(6)]

plotvec_y_7=[R_maj(7),R_min(7)]

plot(plotvec_x_1,plotvec_y_1,plotvec_x_2,plotvec_y_2,'-^',plotvec_x_3,plotvec_y_3,':',plotvec_x_4,plotvec_y_4,'--
',plotvec_x_5,plotvec_y_5,'-.',plotvec_x_6,plotvec_y_6,'-*',plotvec_x_7,plotvec_y_7,'-o')

%plot(vec,R_maj,'*',s,R_min,'o')

legend('ER=0.625','ER=1','ER=2.5','ER=3','ER=3.5','ER=4','ER=5.5')

xlabel('Arclength From Geometric Leading Edge To Blend Point, meters')

ylabel('Radius of Curvature, meters')
```

APPENDIX E. SUPPLEMENTAL FIGURES

Figure 49 represents the variation of leading-edge arclength with ellipticity ratio.

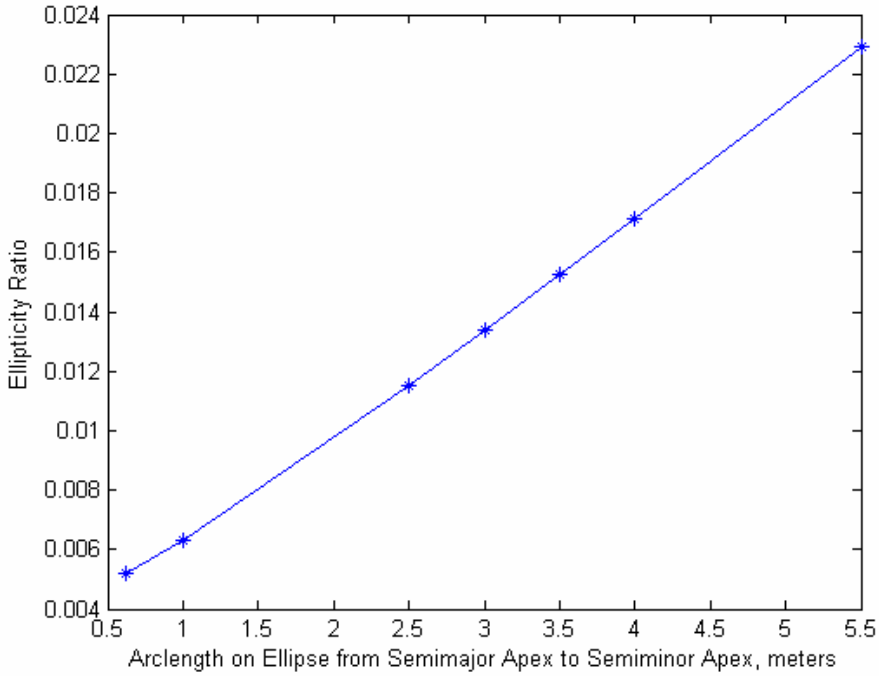

Figure 49. Variation of Elliptical Arclength with Ellipticity Ratio

THIS PAGE INTENTIONALLY LEFT BLANK

LIST OF REFERENCES

1. Walraevens, R. and Cumpsty, N., "Leading Edge Separation Bubbles on Turbomachine Blades," *Proceedings of the ASME, Journal of Turbomachinery*, Volume Number 117, January 1995, pp115-125.

2. Huoxing, L., Baojie, L., Ling, L., and Haokang, J., "Effect of Leading-Edge Geometry on Separation Bubble On a Compressor Blade," Proceedings of ASME Turbo Expo 2003, GT2003-38217, Atlanta, June 2003.

3. Chandrasekhara, M. S., Martin, P. B., and Tung, C., "Compressible Dynamic Stall Control Using Variable Droop Leading Edge Airfoil," *Journal of Aircraft*, Volume Number 41, Number 4, July 2004, pp.862-869.

4. Tuck, E., and Dostovalova, A., "Airfoil Nose Shapes Delaying Leading-Edge Seperation," *The Aeronautics Journal*, Volume Number 104, Number 1039, September, 2000.

5. Park, K., "Numerical Study on the Effects of Blade Leading Edge Shape to the Performance of Supersonic Rotor," Proceedings of AMSE Turbo Expo 2003, GT2003-38292, Atlanta, June 2003.

6. Garzon, V., and Darmafol, D., "Impact of Geometric Variability on Axial Comrpessor Performance," *Journal of Turbomachinery*, Volume Number 125, Number 4, October, 2003, pp692-703.

7. Tuck, E., "A Criterion for Leading-Edge Separation," *Journal of Fluid Mechanics*, Volume Number 222, January 1991, pp.33-37.

8. Abbott, I. H. and Von Doenhoff, A. E., *Theory of Wing Sections*, Dover Publications, 1959.

9. Suder, K., Chima, R., Strazisar, A., and Roberts, W., "The Effect of Adding Roughness and Thickness to a Transonic Axial Compressor Rotor," *Transactions of the ASME, Journal of Turbomachinery*, 1994, 94-GT-339, New York.

10. Reid, L., and Urasek, D., "Experimental Evaluation of the Effects of a Blunt Leading Edge on the Performance of a Transonic Rotor," *Journal of Engineering for Power,* April 1973, Cleveland, pp. 199-204.

11. Tain, L. and Cumpsty, N. A., "Compressor Blade Leading Edges in Subsonic Compressible Flow," *Proceedings of the Institution of Mechanical Engineers*, Volume Number 214, Part C, 2000, pp. 221-242.

12. Calvert, J., "Inviscid-viscous Method to Model Leading Edge Separation Bubbles," *American Society of Mechanical Engineers* (Paper), 1994, 94-GT-247, pp. 1-9.

13. Mason, W. H., "Leading Edge-Trailing Edge Airfoil Interactions," AIAA Paper 95-0436, Blacksburg.

14. Wickens, R. and Nguyen, V., "Wind Tunnel Investigation of a Wing-Propeller Model Performance Degradation Due to Distributed Upper-Surface Roughness and Leading Edge Shape Modification." *Canadian Aeronautics and Space Journal*, Volume Number 38, Number 4, December, 1992, pp. 164-172.

15. Kwon, O., and Sankar, L., "Numerical Simulation of the Flow About a Swept Wing with Leading-Edge Ice Accretions," Computers and Fluids, Volume Number 26, Number 2, November, 1997, pp. 183-192.

16. Broeren, A., Addy Jr., H., and Bragg, M., "Flowfield Measurements About an Airfoil with Leading-Edge Ice Shapes," AIAA Paper, 2004, pp. 5497-5510.

17. Lu, H. and Xu, L., "Circular Leading Edge with a Flat for Compressor Blades," *Journal of Propulsion Technology*, Volume Number 24, 2003, pp. 532-536.

18. Weisstein, E. W., "Ellipse," *Mathworld*, Wolfram Web Resource, http://mathworld.wolfram.com/Ellipse.html, Accessed 23 June 2005.

19. Walker, G. J., "The Role of Laminar-Turbulent Transition in Gas Turbine Engines: A Discussion," *Transactions of the ASME, Journal of Turbomachinery*, Volume Number 115, 1993, pp. 207-217.

20. Mayle, R., "The Role of Laminar-Turbulent Transition in Gas Turbine Engines," *Transactions of the ASME, Journal of Turbomachinery*, Volume Number 113, October 1991, pp. 509-537.

21. Vatsa, V., and Carter, J., "Analysis of Airfoil Leading-Edge Separation Bubbles," *AIAA Journal*, Volume Number 22, Number 12, 1984, pp. 1697-1704.

22. Malkiel, E. and Mayle, R., "Transition in a Separation Bubble," *Transactions of the ASME, Journal of Turbomachinery*, Volume Number 118, October 1996, pp. 752-759.

23. Rosenhead, L., *Laminar Boundary Layers*, Dover Publications, 1988.

24. Schlichting, H. and Gersten, K., *Boundary Layer Theory*, Springer, 2000.

25. Speer, T., "The Basiliscus Project-Return of the Cruising Hydrofoil Sailboat," Chesapeake Sailing Yacht Symposium, pp. 1-22.

INITIAL DISTRIBUTION LIST

1. Defense Technical Information Center
   Ft. Belvoir, Virginia

2. Dudley Knox Library
   Naval Postgraduate School
   Monterey, California

3. Professor Knox T. Millsaps
   Department of Mechanical and Astronautical Engineering
   Naval Postgraduate School
   Monterey, California

4. Professor Garth V. Hobson
   Department of Mechanical and Astronautical Engineering
   Naval Postgraduate School
   Monterey, California

5. Distinguished Professor Anthony J. Healey
   Department of Mechanical and Astronautical Engineering
   Naval Postgraduate School
   Monterey, California

6. Research Professor Muguru S. Chandrasekhara
   Navy-NASA Joint Institute of Aerospace Sciences
   NASA Ames Research Center
   Moffett Field, California

7. Jeffrey S. Patterson
   Gas Turbine Emerging Technologies Section
   NSWC-Carderock Division
   Philadelphia, Pennsylvania